Available online at www.sciencedirect.com
SCIENCE DIRECT®
Biochimica et Biophysica Acta 1656 (2004) 1–31
BIOCHIMICA ET BIOPHYSICA ACTA
BBA
www.bba-direct.com

Review

Microsecond freeze-hyperquenching: development of a new ultrafast micro-mixing and sampling technology and application to enzyme catalysis

Alexey V. Cherepanov, Simon de Vries*

Department of Biotechnology, Delft University of Technology, Julianalaan 67, 2628 BC Delft, The Netherlands

Received 17 July 2003; received in revised form 17 February 2004; accepted 17 February 2004

Available online 14 March 2004

Abstract

A novel freeze-quench instrument with a characteristic «dead-time» of 137 ± 18 μs is reported. The prototype has several key features that distinguish it from conventional freeze-quench devices and provide a significant improvement in time resolution: (a) high operating pressures (up to 400 bar) result in a sample flow with high linear rates (up to 200 m s^{-1}); (b) tangential micro-mixer with an operating volume of ~ 1 nl yields short mixing times (up to 20 μs); (c) fast transport between the mixer and the cryomedium results in short reaction times: the ageing solution exits the mixer as a free-flowing jet, and the chemical reaction occurs "in–flight" on the way to the cryomedium; (d) a small jet diameter (~ 20 μm) and a high jet velocity (~ 200 m s^{-1}) provide high sample-cooling rates, resulting in a short cryofixation time (up to 30 μs). The dynamic range of the freeze-quench device is between 130 μs and 15 ms. The novel tangential micro-mixer efficiently mixes viscous aqueous solutions, showing more than 95% mixing at $\eta \leq 4$ (equivalent to protein concentrations up to 250 mg ml^{-1}), which makes it an excellent tool for the preparation of pre-steady state samples of concentrated protein solutions for spectroscopic structure analysis. The novel freeze-quench device is characterized using the reaction of binding of azide to metmyoglobin from horse heart. Reaction samples are analyzed using 77 K optical absorbance spectroscopy, and X–band EPR spectroscopy. A simple procedure of spectral analysis is reported that allows (a) to perform a quantitative analysis of the reaction kinetics and (b) to identify and characterize novel reaction intermediates. The reduction of dioxygen by the bo_3-type quinol oxidase from *Escherichia coli* is assayed using the MHQ technique. In these pilot experiments, low-temperature optical absorbance measurements show the rapid oxidation of heme o_3 in the first 137 μs of the reaction, accompanied by the formation of an oxo-ferryl species. X-band EPR spectroscopy shows that a short-living radical intermediate is formed during the oxidation of heme o_3. The radical decays within ~ 1 ms concomitant with the oxidation of heme *b*, and can be attributed to the $\mathbf{P_M}$ reaction intermediate converting to the oxoferryl intermediate **F**. The general field of application of the freeze-quench methodology is discussed.

Keywords: Pre-steady state kinetics; Freeze-quench; Hyperquenching; Transient intermediate; Cytochrome bo_3 oxidase; Radical; Myoglobin

1. Introduction

Kinetic analysis of enzyme-promoted chemical reactions is an important approach in biological chemistry, which is used to define, characterize, and elucidate the chemical mechanics of biocatalysis. Since the seminal work in this field by Fischer in 1894 [1], and Michaelis and Menten in 1913 [2], countless numbers of proteins have been studied and their catalytic properties described and characterized well [3,4]. However, despite the wide and acclaimed use of this approach, the fundamental problem remains in general unsolved: the *direct experimental correlation* between the kinetics of the chemical reaction and the spatially well-defined dynamics of the enzyme structure cannot be established. The reason stems from the lack of experimental techniques for both preparation of the transient kinetic samples and analysis of their structures.

In this paper, we review and report the latest advances in mixing-and-sampling technology that bring freeze-quenching forth as a potential method of choice to prepare transient kinetic samples for structural analysis.

In general, freeze-quenching is a three-stage process, which gives a unique opportunity (a) to initiate/synchronize a chemical reaction by rapidly mixing the reaction components, (b) to vary the reaction time by delivering a sample to

* Corresponding author. Tel.: +31-15-2785139; fax: +31-15-2782355.
E-mail address: S.deVries@tnw.tudelft.nl (S. de Vries).

0005-2728/$ - see front matter © 2004 Elsevier B.V. All rights reserved.
doi:10.1016/j.bbabio.2004.02.006

the cryomedium after different time intervals, and (c) to capture transient intermediates by suddenly freezing the reaction mixture. Freeze-quenched samples can be stored at low temperatures for a long period of time, and their structure can be analyzed using different spectroscopic techniques.

The success of the method depends on two key parameters. It is essential (a) to vary the reaction time in a wide range (μs–ms–s), so that the entire turnover of an enzyme can be assessed, and (b) to minimize the temporal "dilution" of transient kinetic intermediates. To achieve the latter, the mixing of the reaction components, the diffusion-dependent binding, and the cryofixation of the reacting sample have to be set considerably faster than the first-order catalysis. Ideally, all second-order events should be over within the time of mixing, while the first-order events should not have yet started. Under these circumstances, there is a chance to observe a "slide show" of reaction intermediates as the sample moves towards the cryomedium, where the intermediates are captured by rapid freezing.

In general, proteins in solution experience a wide spectrum of dynamic fluctuations that span the time scales from femtoseconds to milliseconds, involving residues that are located at the protein–solvent interface or are immersed in the protein matrix [5–7]. Molecular tumbling of the protein molecule [8,9], "breathing" [10], motions of the side chains of individual residues [6,7,11], movements of secondary, tertiary, and quaternary structure elements [12,13] can all be distinguished [14–16]. In addition, the proteins may undergo rapid disorder-to-order transitions, e.g. ordered state–molten globule–random coil upon binding and catalysis [17]. On the other hand, chemical catalysis in this multifactorial system rarely occurs with turnover numbers higher than 10^6 s^{-1} [18–20], with the exception of some rapid light-driven biological processes [21–28]. Thus, the specific conformational changes that the enzymes are using to steer the chemical events during catalysis, and that are of primary interest for the structural analysis, are mainly confined to the micro- and millisecond time domain. There are many examples, when the motions of the primary and/or secondary structure elements with characteristic times of 10^{-2}–10^{-6} s were observed and assigned to a particular step of chemical catalysis [29–40]. Triosephosphate isomerase is a representative example, where a motion of a single 10-residue-long loop in the active site of the enzyme controls the entire catalytic cycle, facilitating, in an open form, binding and release of a ligand, and, in a closed form, controlling the formation and protecting the reaction intermediates [41–43]. Another example involves cyclophilins, where the dynamics of a single arginine residue plays a critical role in the catalysis of the *cis*/*trans* isomerization of peptidyl/prolyl bond during catalysis [44,45]. Dihydrofolate reductase is the enzyme that catalyzes the NADPH-dependent reduction of 5,6,7,8-tetrahydrofolate, the essential component for the biosynthesis of purines and certain amino acids. In this enzyme, the mobility of two loops (*Met*20 and *βF-βG*) was shown to control the formation of the enzyme–substrate Michaelis complex, as well as to regulate the release of the product [6,46–48].

In relation to the freeze-quenching method, these and other examples of structural enzyme kinetics pose clear time limitations on the three main steps of the sample preparation process. To avoid "dilution" of conformational intermediates, mixing and cryofixation of the sample should occur within 1–10 μs, while the sample-transport "dead" time should not exceed 10–100 μs. An overview of the current state of the freeze-quenching technology leads to the conclusion that none of the individual steps of the sample preparation process comply with these essential requirements. Taking as example the "Ballou" freeze-quench instrument reported in Refs. [49,50], the minimal sample mixing time can be estimated as ~1 ms, the transport time 1–2 ms, and the time of cryofixation, owing to the low linear velocity of the sample flow and large jet diameter, as long as 2 ms [51,52]. As a result, the characteristic "dead" time of sample preparation for this and similar commercially available devices is around 5 ms [53–57].

Despite its low time resolution, the conventional "rapid" freeze-quench technique (RFQ) is widely used, and a wealth of mechanistic studies have been performed on the catalysis and reactivity of metal centers in biological systems [58–69], in particular the studies on bioreduction of molecular oxygen [53,70–75]. As a well-characterized example, carboxylate-bridged diiron(II) cluster can be brought forth, the reaction center that defines the *modus operandi* of a wide class of proteins, ribonucleotide reductases (RNR), such as class I RNR from *E. coli* [76,77], bacterial hydrocarbon hydroxylases, such as soluble methane monooxygenase (MMO) from methanotrophs *Methylococcus capsulatus* and *Methylosinus trichosporium* [78–80], ferritins [81–83], and plant fatty acyl desaturases, such as stearoyl acyl carrier protein Δ^9-desaturase from castor seeds [84,85]. The diiron reaction center catalyzes the reductive oxidation of molecular oxygen, which is slow compared with the similar reaction of a binuclear iron-copper center of cytochrome *c* oxidase [86–95], and thus it is accessible for mechanistic studies using the RFQ technique. The mechanism of dioxygen reduction by the diiron (II) cluster is quite complex; it includes several reaction intermediates, and involves both short- and long-living radical species. Taking the example of RNR, activation of the molecular oxygen leads to the formation of the dinuclear ferric cluster-tyrosyl radical cofactor [96–98]; the latter generates the catalytic thiyl radical via long-range coupled electron and proton transfer [99–101], essential for the reduction of the ribonucleotide [102–104]. The four-electron O_2 reduction proceeds via the formation of a transient tryptophan cation radical ($\mathbf{W}^{+\cdot}$) and the mixed valence Fe(III)/Fe(IV) species (**X**) [88,105–

107]. It was proposed that the peroxydiiron(III) intermediate similar to compound **P** of MMO [90,108,109] precedes the $\mathbf{XW}^{+\cdot}$ diradical species along the reaction coordinate [86,110–113], though, not without a controversy [88]. The existence of a "kinetically masked" non-covalent O_2-bound diiron(II)-intermediate [88] (similar to the compound **A** of cytochrome *c* oxidase [114]) has been suggested [106].

For a detailed understanding of the reaction mechanism of the protein–metal redox reaction center, it is pertinent to follow the time-resolved changes of (i) metal oxidation states, (ii) metal–ligand and metal–metal bond lengths, (iii) ligand–ligand and metal–ligand bond stretching frequencies, and (iv) the nature of the catalytic radicals. For this purpose, in the case of the carboxylate-bridged diiron(II) cluster RFQ sampling has been coupled to sample analyses by UV–Vis absorbance, EPR, ENDOR, EXAFS, resonance Raman, and Mössbauer spectroscopy. Combined data from UV–Vis, RFQ-EPR and RFQ-Mössbauer analyses allowed detection and characterization of the tryptophan cation radical, as well as to show that it is formed simultaneously with the mixed valence intermediate **X** [88,105,115], donating the fourth electron for the reduction of oxygen [106]. Use of RFQ-EPR allowed detection and characterization of the mixed valence intermediate **X** [105,116–118], tyrosyl- [105,117,118], and thiyl- [104,119,120] radicals. Mössbauer studies [105,115,118,121], coupled with resonance Raman and EXAFS analyses [122,123], supported by the ENDOR results [116,124–126], allowed structural identification of **X**, and μ-(oxo)diiron(III) species in the diferric tyrosyl radical cofactor [88]. Unfortunately, the low time resolution of RFQ technique has left several questions unanswered. Perhaps, a submicrosecond time resolution, such as reported in this paper for the MHQ technique, is required to capture and characterize a non-covalent O_2-bound diiron(II)-intermediate, which was implied for MMO on the basis of kinetic studies [88] but has not been observed so far in the case of RNR. The same holds for the isolation and identification of the structure of the peroxy-intermediate for the wt RNR, which has been postulated/reported in Refs. [86,110,112,113] and disputed in Refs. [88,127].

In 2002 we have reported the development of a novel method of microsecond freeze-hyperquenching (MHQ)—a breakthrough in technology that led to a 50-fold increase in time resolution over conventional rapid freeze-quenching [128]. In the present work we describe in detail the further advancements in the MHQ technology and instrumentation, and provide a general introduction to the freeze-quench mixing-and-sampling, discussing (i) a strategy for improving the overall time resolution of the freeze-quench process, (ii) a new design of the mixer and the freeze-quench instrument, (iii) characterization of the novel freeze-quenching device using the reaction of binding of azide to metmyoglobin from horse heart, and (iv) application of the method to study the mechanism of dioxygen reduction catalyzed by the bo_3-type quinol oxidase from *E. coli*.

2. Review, results and discussions

2.1. Freeze-quench technology—problems and solution strategy

In general, the freeze-quench mixing-and-sampling technique can be viewed as a three-stage process. At the first stage, the chemical reaction is initiated by rapid mixing of the reaction components. The reaction chemistry occurs during the second stage, when the sample is transported from the mixer to the cryomedium surface. At the third stage, the reacting sample is suddenly frozen in the cryomedium, and the chemical reaction is captured in some intermediate state [129–132].

The characteristic sample-ageing time, τ_a, can thus be resolved into three terms,

$$\tau_a = \tau_m + \tau_t + \tau_c \quad (1)$$

τ_m is the mixing time, τ_t is the sample-transport time, and τ_c is the cryofixation time.

Below, we pinpoint and discuss the limitations of each stage of the freeze-quench process, as well as outline the solution strategy that was used in the present work.

2.1.1. Mixing

Two main parameters determine the time resolution of the mixing process, (i) the sample flow rate, and (ii) the operating volume of the mixer [133].

In the conventional freeze-quench devices [49,50,53,55,132], the mixing time is quite long, $\tau_m \sim 1$ ms even at

Table 1
Technical specifications of the MHQ instrument vs. previous apparatus [49,50]

		This work	[49,50]
Pre-mixing volume, nl		1±0.1	960
(μm)		(120×120×60)	(1588×1588×381)
Mixing volume, pl		10±1	6.8×10^4 (68 nl)
Orifice diameter, μm		20±1	330
*Re**	pre-mixing chamber	<1000	<5000
	Orifice	<4000	<7000
Backpressure, bar (psi)		0–417 (0–6000)	~0–5 (0–70)
Flow rate, ml min^{-1}		0.4–3.6	36–109
Jet speed, m s^{-1}		20–200	1–10[‡]
Spraying distance, cm[†]		2–30	>2
Dynamic range, ms		0.1–14	>5

[†] With liquid cryomedium.
[‡] Linear flow rate in the sample delivery tubing.
* Reynolds number.

high sample flow rates (~ 1 ml s^{-1}), owing to a relatively large mixing volume (~ 1 μl, Table 1).

For continuous-flow experiments, a device has been reported that combines both a small mixing volume and high rates of the sample flow [134]. It is based on the design by Regenfuss et al. [135,136], where the principle of coaxial mixing [137] is combined with the Berger-type ball mixing [138,139], the dimensions of the mixer are scaled down to a mixing volume of ~ 9 nl, and the flow rates are kept high (~ 0.6 ml/s). As a result, the mixing time is estimated as τ_m ~ 15 μs [134], satisfying the requirements for the preparation of transient reaction samples mentioned in Introduction. However, to our opinion the design of the coaxial-ball micromixer makes it inherently impractical for the operation on a day-to-day basis if compared to the other glass/quartz-free designs. The coaxial micromixer contains fine internal parts of custom design, which might be too fragile for operation in vacuo at sample-delivery pressures of 0.1–0.4 kbar. Thus, in this work we have pursued a different approach, which was first introduced by Hartridge and Roughton [133,140–142] in 1920s using the modified Rolls Royce carburetor for mixing the reaction components. The approach is based on the principle of alternating multi-stream mixing of the reaction components resulting in an angular momentum (tangential mixing). The four-jet tangential mixers are extensively used for freeze-quench experiments, and are known for their robustness, reliability and high mixing efficiency [49,50,57,132,143].

The challenge of this work was to design and machine a four-jet tangential mixer with a mixing volume small enough to reach the required τ_m values (~ 10–20 μs).

In summary, the dimensions of the mixer have been scaled down roughly 10-fold with respect to the "Ballou" design [49,50], resulting in a ~ 10-fold decrease of the operating volume (to ~ 1 nl) with respect to the coaxial-ball mixer [134], a decrease of the jet diameter to ~ 20 μm, and an increase of the jet speed to ~ 200 m s^{-1} (Table 1). The sample preparation time has increased from ca. <0.3 to 12–90 s, giving more possibilities to control the quality of the sample preparation process in situ.

2.1.2. Transport

The sample transport rate is determined by two critical parameters, (i) the linear flow rate–pressure in the system, and (ii) the distance between the mixer and the sampling area.

In the conventional setup, the sample-transport time, τ_t, has intrinsically a large value because of the relatively low linear flow rates (<20 m s^{-1}), large mixer dimensions/diameter of the sample-delivery tubing, long transport distance (~ 1–2 cm), and low operating pressure (<5 bar, 70 psi) [49,50,73,132]. Thus, to achieve 5-ms time resolution, the volumetric flow rate has to be kept rather high (~ 1 ml/s, Table 1).

The increase of the linear flow rate allows a dramatic improvement of the time resolution, e.g. at a 200 m s^{-1} flow rate the transport time over l = 20 mm is as short as 100 μs. Acceleration of the sample flow is associated with pressure increase (Fig. 1), a serious technological problem, which requires re-design of the entire freeze-quench set up. For example, for a 200 m s^{-1} sample flow, the pressure

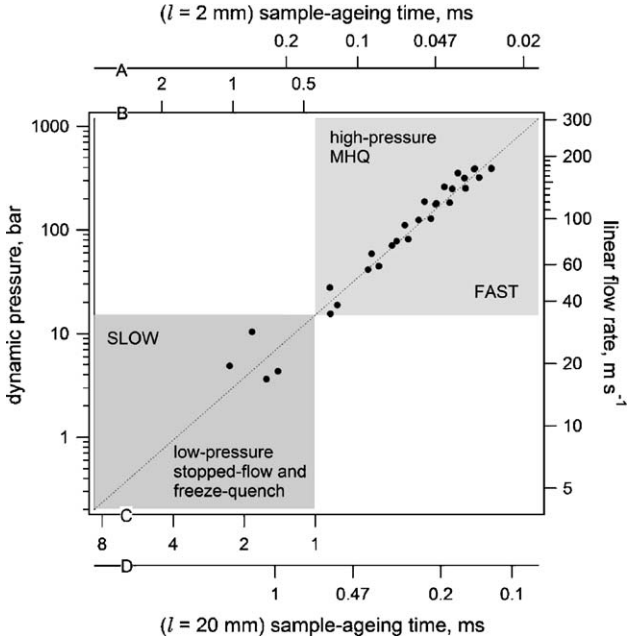

Fig. 1. Dependence of the sample-ageing time on the linear flow rate of the sample and the operating pressure of the mixing-and-sampling instrument. The correlation between dynamic pressure and the linear flow rate (dotted trace) was obtained by fitting Eq. (2) to the experimental data (solid circles) (with kinetic energy coefficient α = 2, and friction coefficient C_v = 0.88 ± 0.03). Dynamic pressure in the mixer was measured as a function of the volumetric flow rate. The values of the linear flow rate have been calculated using the values of the volumetric flow rate and the orifice diameter, plus the 10% increase of the linear flow velocity as measured by LDA. Axes (A, D)—sample-ageing time calculated for the MHQ setup reported in this work (mixer volume—1 nl, the diameter of the mixer orifice and the sample jet d = 20 μm, distance between the mixer and the cryomedium l = 2 and 20 mm, respectively). Axes (B, C)—sample-ageing time calculated for the low-pressure stopped-flow (B) and freeze-quench (C) instruments (stopped-flow: mixer volume—1 μl, volume of the sample cuvette—10 μl, distance between the mixer and the cuvette l = 2 mm with a diameter of 1 mm, total sample filling volume of 13 μl; freeze-quench: as reported in Refs. [49,50], mixer volume—1 μl, the diameter of mixer orifice and sample delivery tubing d = 0.3 mm, distance between the mixer and the cryomedium surface l = 20 mm). Sample-ageing time was calculated by adding the mixing time (the time it takes for the sample to fill the mixer volume) and the time of sample delivery (calculated as the time it takes for the sample with the denoted linear flow rate to travel over the distance l between the mixer and the cryomedium. In case of the stopped-flow, the time it takes to fill the sample observation cuvette is added. Note that the freezing time was left out from the total sample-ageing time, enabling comparison between the two methods (stopped-flow and freeze-quench). Low-pressure freeze-quench and stopped-flow devices are operating at pressures <15 bar; high-pressure instruments may operate up to ~ 1 kbar; operational rate–pressure–time areas for both low- and high-pressure instruments are denoted with gray.

Table 2
Kinetic parameters of the reaction of the horse heart metmyoglobin with azide at 5 °C and different pH values

pH	Apparent rate constant	Low $[N_3^1{}^-]$ (<1 mM)	High $[N_3^1{}^-]$ (>10 mM)	k_{low}/k_{high} †*
4	k_1^{app}, M^{-1} s^{-1}	$9.3 \pm 0.06 \times 10^4$	$5.7 \pm 0.2 \times 10^3$	16.3
	k_{-1}^{app}, s^{-1}	$5.7 \pm 0.7 \times 10^{-2}$	83 ± 8	1460*
	K_d^{app}	0.61 ± 0.08 μM	15 ± 1 mM	2.4×10^4*
5	k_1^{app}, M^{-1} s^{-1}	$2.99 \pm 0.04 \times 10^4$	$3.5 \pm 0.1 \times 10^3$	8.5
	k_{-1}^{app}, s^{-1}	$1.35 \pm 0.08 \times 10^{-1}$	57 ± 6	420*
	K_d^{app}	4.5 ± 0.1 μM	16 ± 6 mM	3600*
5.5	k_1^{app}, M^{-1} s^{-1}	$1.29 \pm 0.01 \times 10^4$	$1.48 \pm 0.05 \times 10^3$	8.7
	k_{-1}^{app}, s^{-1}	$1.37 \pm 0.05 \times 10^{-1}$	57 ± 3	420*
	K_d^{app}	10.6 ± 0.6 μM	38 ± 3 mM	3600*

†k_{low}—rate constant at low $[N_3^1{}^-]$, k_{high}—ibid. at high $[N_3^1{}^-]$. *For k_{-1}^{app} and K_d^{app} the ratio is inverted, k_{high}/k_{low}.

build-up in the mixer is ~0.5 kbar. The experimental values follow the Bernoulli's velocity/dynamic pressure correlation (2) (Fig. 1, dotted trace).

$$\Delta P = \alpha \frac{\rho U^2}{2C_v^2} \quad (2)$$

ΔP is the pressure build-up in the orifice, α is the kinetic energy coefficient ($\alpha = 2$ for laminar flow, or 1.01–1.1 for fully developed turbulent flow), ρ is the liquid density, U is the linear velocity at the orifice, C_v is the wall friction coefficient, $C_v = \frac{U}{U_{max}}$, and $U_{max} = \sqrt{\frac{2\Delta P}{\alpha\rho}}$.

The high friction in the orifice ($C_v = 0.88 \pm 0.03$ vs. ~0.97–0.99 for normal flows, see legend to Fig. 1) can possibly be attributed to the pronounced wall effects in the micro-mixer with dimensions of 20–120 μm.

From Fig. 1 it also becomes clear that the low-pressure "stopped-flow type" of sample preparation that involves pneumatically driven glass Hamilton syringes for the sample delivery at pressures <15 bar, is inherently limited to the time range of >0.5 ms (over 2 mm) or >1 ms (over 2 cm). The use of the high-pressure "HPLC-type" systems becomes inevitable with entering the microsecond time domain. In this light, two recent reports where the sample-ageing time of 200 μs has been claimed in a low-pressure instrument [144,145], to the authors' opinion, has to be critically evaluated. A few key points can be mentioned as follows. Glass Hamilton syringes (5 ml) have been used for the sample delivery (maximum operating pressure 200 psig/15 bar) while, under the described conditions, the pressure in the system is expected to be 30–60 bar (Eq. (2), also see Fig. 1). The reacting sample has been delivered to the cryomedium as a small-diameter high-speed free-flowing jet (~50–60 μm diameter, ~50–70 m s^{-1} velocity). However, any slow-down/break-up of the jet due to air resistance that leads to an increase of the delivery time has not been considered. In addition, cooling of the jet due to heat exchange with air in the vicinity of the rapidly rotating cold plate/LN_2 surface has not been evaluated (~1 krpm rotation speed, <1 cm distance). This factor plays an important role in decreasing the jet temperature to ~8 °C in our freeze-quench setup, even though we have two- to fourfold faster jets. Tanaka et al., as well as other researchers that develop ultrafast freeze-quenching devices [146], use the metmyoglobin–azide reaction as the molecular timer to calibrate the freeze-quench instrument. However, a ~10-fold decrease of the apparent binding rate constant at high azide concentrations (>1 mM, Tables 2 and 3) is not taken into account, as well as the slow-down of the binding reaction due to decrease of the jet temperature. Both of these factors lead to "underreaction" of the freeze-quench sample, resulting in the apparent "shortening" of the

Table 3
Kinetic and thermodynamic parameters of the reaction of the horse heart metmyoglobin with azide at pH = 5 and 20 °C

$[N_3^1{}^-]$ <1 mM K_d^{app}, M $14.9 \pm 0.5 \times 10^{-6}$			
k_1^{app}, M^{-1} s^{-1}	$9.57 \pm 0.08 \times 10^4$	k_{-1}^{app}, s^{-1}	1.43 ± 0.03
E_A^1, kcal/mol	$\Delta S_1^{\#}$, cal deg^{-1} mol^{-1}	E_A^{-1}, kcal/mol	$\Delta S_{-1}^{\#}$, cal deg^{-1} mol^{-1}
9.2 ± 0.1	-6.2 ± 0.5	16.9 ± 0.4	-2.3 ± 1.4
$[N_3^1{}^-]$ >10 mM K_d^{app}, M $28.7 \pm 1.2 \times 10^{-3}$			
k_1^{app}, M^{-1} s^{-1}	$1.49 \pm 0.15 \times 10^4$	k_{-1}^{app}, s^{-1}	$4.3 \pm 0.6 \times 10^2$
E_A^1, kcal/mol	$\Delta S_1^{\#}$, cal deg^{-1} mol^{-1}	E_A^{-1}, kcal/mol	$\Delta S_{-1}^{\#}$, cal deg^{-1} mol^{-1}
15.8 ± 1.3	12.5 ± 4.5	18.8 ± 1.5	15.6 ± 5.4

The values have been determined using the experimental data shown in Fig. 8.

sample-ageing time. In addition, the pH of the metmyoglobin–azide reaction mixture in the assay, a critical value that defines the binding rate constant, has not been specified. Finally, Tanaka et al. use a single freeze-quench sample for the determination of the instrument "dead" time.

In our opinion, the real "dead-time" of the freeze-quench instrument reported in [144,145] is between 0.8 and 1 ms, which is nevertheless a five- to sixfold improvement in time resolution with respect to the "Ballou" design.

Decreasing the distance between the mixer and the cryomedium allows an additional improvement of the time resolution of the freeze-quench set up, which, similar to increasing the linear flow rate, requires a major redesign of the instrumental setup. Use of a liquid medium (i.e. isopentane) for cryofixation at high jet velocities ($\sim$ 50–200 m s^{-1}) poses a limitation of $l \sim 2$ cm on the distance between the mixer and the cryomedium. Freeze-quenching at shorter distances yields inhomogeneous sampling due to "splashing" of the cryomedium during spraying, nozzle blockage and freezing of the sample in the mixer. It appears a prerequisite to use a solid cryomedium in order to decrease the transport distances and the delivery times to 2–3 mm/30–40 μs (Fig. 1). Cryofixation on a cold plate gives rise to several technical problems that involve rotation of the cold plate, actuation of the mixer, and delivery of the rotation motion into the vacuum chamber. We have designed and assembled a prototype cold-plate MHQ instrument (A. Cherepanov and S. de Vries, unpublished); the characterization of the device, optimization of the quenching conditions, and determination of the sample-ageing time are currently in progress.

In this work, we use isopentane as the cryomedium, so the minimal transport distance is set to 20 ± 2 mm. The jet velocity is high, <200 m s^{-1}; thus, the minimal overall sample transport time is $\sim$ 100 μs (Fig. 1, Table 1).

2.1.3. Freeze-quenching

Two main parameters determine the kinetics of the freezing process, the speed of the sample jet, and the jet diameter [147].

It was previously shown that the spraying of fast jets ($\sim$ 200 m s^{-1}) of small diameters (10–20 μm) into a liquid cryomedium (isopentane at 120 K) [148] results in cooling rates of at least 3×10^6–10^7 deg s^{-1} (based on calculations in Refs. [149,150]). Under these circumstances, water does not have time to form a crystal lattice, and vitrifies to the amorphous solid water (ASW), bypassing the liquid–ice phase transition [147,148]. In terms of its structure, metastable ASW is directly related to liquid water [151–156], and, at a temperature of approximately 130 K it undergoes a reversible, thermodynamically continuous liquid–liquid transition [157], forming a highly viscous, deeply metastable supercooled extension of normal liquid water [158–160], which crystallizes only on warming to $\sim$ 160 K [161,162]. Vitrification of samples is widely used in cryobiology for (a) tissue storage and cryopreservation, and (b) preparation of samples for electron microscopy, to avoid structural damage of the biological specimen due the expansion of the aqueous phase during the liquid–ice phase transition [163–166].

In the present work, we followed the vitrification conditions described in Ref. [148], to ensure that the sample is freeze-quenched within $\sim$ 30 μs after it contacts the cryomedium. In comparison, the cryofixation time of the conventional freeze-quench setup is almost 100-fold longer, $\sim$ 2 ms [51]. The general reasons for that are, (i) a 10–20-fold larger diameter of the sample jet (0.3–0.4 mm), and (ii) an order of magnitude lower jet velocity (1–10 ms^{-1}). Both of these factors seems to limit the heat transfer rate from the cryomedium to the sample droplets.

Summarizing the strategy of improving the time resolution of the freeze-quench process, in the present work we attempted (a) to minimize the mixing time, (b) to minimize the sample transport time, and (c) to increase the heat transfer rate during cryofixation. Along these lines of consideration, the following modifications have been introduced in the design of the freeze-quench instrument: (a) the mixer dimensions were scaled down, (b) the operational pressure was increased, and (c) the sample-delivery tubing was omitted.

2.2. Description of the MHQ setup

In the current setup (Fig. 2), the sample exits the mixer as a free-flowing jet of a small diameter ($\sim$ 20 μm) (Fig. 2-4,5). Depending on the volumetric flow rate, the jet speed can reach values up to $\sim$ 200 m s^{-1}.

The sample is injected into the mixer through the high-pressure sample injection valve (Rheodyne type) using the HPLC-type solvent delivery pumps with operational pressures between 1 and 415 bar (14–6000 psi) (Fig. 2-12, 13-1,13-2).

To minimize the slow-down and break-up of the jet at linear flow rates above 20 m s^{-1}, both mixer and cryomedium are mounted inside a low pressure chamber (Fig. 2-1), which is operated at pressures 0.5–100 mbar (Table 1). Low pressure ensures that the jet speed is constant along the distance between the mixer and the cryomedium.

The characteristic feature of the novel freeze-quench device is a continuous-flow *modus operandi*. It stems from the necessity to carry out the consecutive sample-preparation events in a reproducible way. A dry start of the sample flow under vacuum results in the eventual clogging of the orifice, sometimes even before injection of the sample. This is another reason, besides the high-pressure requirement, why the sample delivery has been changed from the pulsed-flow-type to the HPLC-type injection mode.

After injection, the reaction sample is sprayed into the vial (Fig. 2-7) containing cold isopentane at 125 K. To ensure homogeneous freeze-quenching, the cryomedium is stirred vigorously with an external magnetic stirrer (Fig.

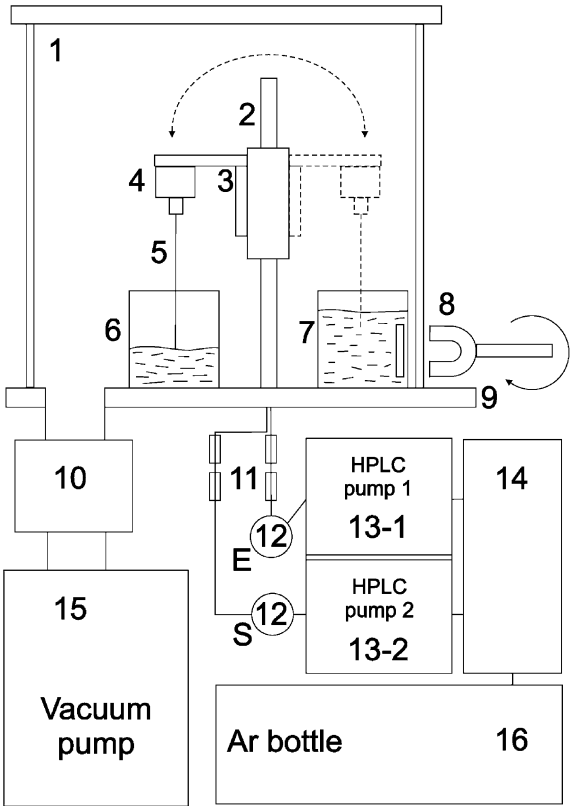

Fig. 2. Schematics of the freeze-quenching setup. 1—Low-pressure chamber; 2—stainless steel rod holder; 3—90° bracket holder; 4—tangential micro-mixer; 5—sample jet; 6—solvent collection vessel; 7—sample collection vessel; 8—magnetic stirrer; 9—low-pressure chamber base plate; 10—LN_2-cooled vapor trap; 11—5-μm and 0.2-μm in-line solvent filters; 12—Rheodyne-type sample injection valves; 13-1, 13-2—HPLC-grade solvent delivery pumps; 14—carrier solvent vessel; 15—RV5 oil vacuum pump; 16—compressed *Ar* gas vessel. All fluid and gas transport lines are equipped with HPLC-grade PEEK tubing and high-pressure ferrule connections (15 kpsi). The carrier-solvent vessel (14) is purged with *Ar* (16) to maintain anaerobic conditions. Two HPLC-grade pumps (13-1, 13-2), installed in parallel, are used to deliver the carrier solvent to the micro-mixer (4), bypassing the "enzyme" and "sample" injection valves (12). The solution enters the low-pressure chamber (1) as a free-flowing jet (5). In the purging mode, the jet is collected in the solvent collection vessel (6). In the operation mode, the reaction sample is sprayed into the sample collection vessel (7), filled with cold isopentane (150 K). During collection, the isopentane is vigorously mixed by the magnetic stirrer (8). To initiate the collection of the sample, the swinging arm (3) is rotated in the low-pressure chamber by an external magnet. For further comments, see text.

2). The sample-ageing time can be varied by changing both the jet velocity and the jet length. After freeze-quenching of the sample, the isopentane-sample slurry is transferred to the cold bath equilibrated at 125 K. The slurry is used for the analysis by low temperature optical absorbance spectroscopy without additional treatment. For X-band EPR spectroscopy, the sample suspension is concentrated and packed in the EPR tube in a cold centrifugation setup (see Experimental procedures).

In summary, the reaction chemistry is initiated in a four-jet tangential micro-mixer. The mixed solution is injected into a low-pressure chamber as a high-speed free-flowing jet of a small diameter. The components react while the jet travels from the mixer to the surface of the cryomedium, where the reaction intermediates are captured after a sudden freezing of the reaction sample. In the present work, samples are analyzed by low temperature optical absorbance spectroscopy, or X-band EPR spectroscopy.

2.3. Principle, design, and dimensions of the novel four-jet tangential micromixer

The principle of a novel four-jet tangential mixer is based on earlier designs reported in [49,50,132,140,143] (Fig. 3).

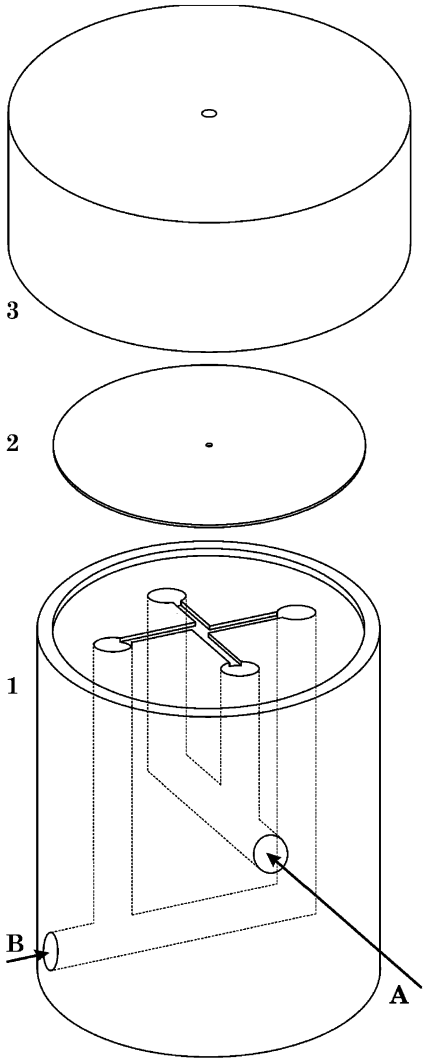

Fig. 3. Schematic drawing of the novel tangential micro-mixer. 1—Mixer body; 2—platinum inlay with the orifice; 3—brass screw-in cap. Reaction components A and B enter the mixer body as indicated; they are filling the mixing volume passing through four channels arranged in the cross geometry, in which each channel is offset with respect to the opposite one for half-width of the channel. Components are forced through a narrow orifice in the platinum inlay and the opening in the brass screw-in cap into the low-pressure chamber.

In short, the micromixer is composed of four channels (arranged in a X-form geometry), which are leading the reaction components to the pre-mixing chamber positioned in the middle of "X" (Fig. 3-1). The opposite channels are offset in respect to each other by the half-width of the channel, so that the liquid streams are pre-mixed with a resulting angular momentum at relatively low Reynolds numbers ($Re < 1000$). After pre-mixing, the four-stream solution is forced through a narrow orifice (Figs. 3-2 and 4-I-3) to the sample delivery tube [49,50,132], or, in our setup, directly into the low-pressure chamber, in a direction perpendicular to the plane of the channels. The solution in the orifice is accelerated to a high linear velocity, and the mixing of the reaction components takes place at moderate Reynolds numbers ($Re \sim 4000$).

Compared to the "Ballou" design, the distinguishing feature of the novel mixer is an alternating sequence of the sample channels (ABAB versus AABB, see Fig. 3-1), which provides high mixing efficiency of the reaction components. In addition, the dimensions of the mixer are scaled down roughly 10-fold. For example, the channels leading to the pre-mixing chamber are 60 ± 5 μm wide and of similar depth. The pre-mixing chamber is approximately rectangular with dimensions $120 \pm 10 \times 120 \pm 5 \times 60 \pm 5$ μm (Figs. 3 and 4-I,II). The flat surface, which bears the engraved channels and pre-mixing chamber, is covered with a 100-μm-thick platinum inlay with an orifice in the middle (Fig. 3-2). When the inlay is mounted inside the mixer head (Fig. 3-1), the orifice is positioned opposite to the center of the pre-mixing chamber. The orifice geometry is depicted in Fig. 4-I. It has a cylindrical shape with a diameter of 20 ± 1 μm and a length of 33 ± 1 μm, providing a mixing volume of ~ 10 pl. The solution enters the orifice through a cut-conical area with a depth of 67 ± 1 μm and a diameter of approximately 100 μm. Together with the indentation in the mixer body, it forms the walls of the pre-mixing chamber (Fig. 4-I-3), which has a volume of ~ 1 nl (Table 1).

The platinum inlays with different orifice diameters, i.e. 5, 10, 20, 30 50 and 100 μm are commercially available. We are using primarily inlays with a 20-μm-orifice, which is the most versatile for use, giving stable backpressure and low clogging frequency during sample injection and/or short-term storage in the assembled state (up to 3 days).

The platinum inlay is secured on the top of the mixer head with a brass screw cap (Fig. 3-3). It has a 0.3-mm-wide orifice in the middle, which allows the jet to exit the mixer (Fig. 4-III).

2.4. Estimation of the duration and the efficiency of mixing

2.4.1. Mixing time

Chemical reaction initiated in the mixing-and-sampling instrument starts in the course of micromixing of the reaction components [167,168]. In relation to the tangential mixer, it is important to understand whether this process takes place already in the pre-mixing chamber, or in the orifice, where the solution is accelerated to a high linear velocity. It is essential to pinpoint the mixing place, because the resulting τ_m value could differ roughly by two orders of magnitude. For example, if the reaction

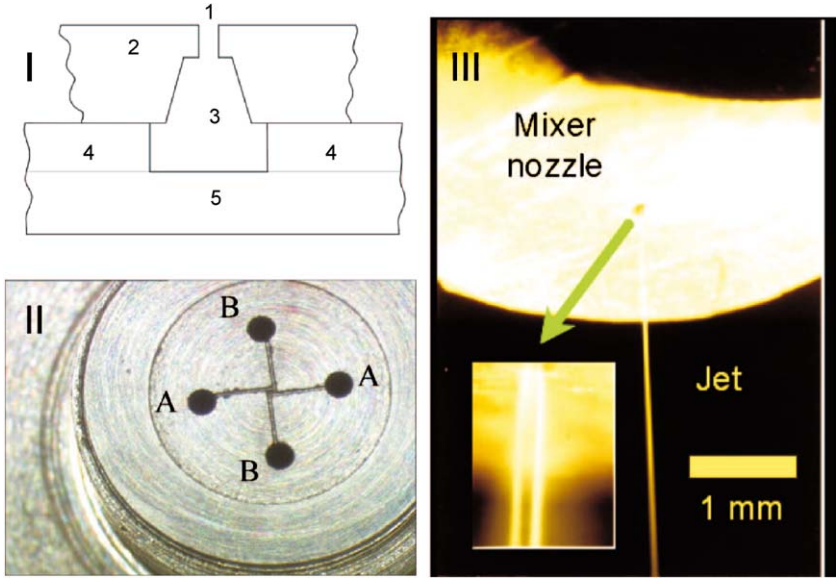

Fig. 4. Images of the micro-mixer, and the geometry of the (pre)mixing chamber. (I) The slice through the mixer body (5), and the platinum inlay (2) along the two channels (4) (A–A, or B–B, see **II**). The pre-mixing chamber (3) is confined between the indentation in the mixer body, and the narrow orifice (1) in the platinum inlay cover. **(II)**—Dismounted mixer showing the channels and the pre-mixing chamber. Letters relate to the two-component-mixing, A + B. The components enter the pre-mixing chamber through the channels in the alternating way (ABAB). **(III)**—Assembled mixer (with mounted platinum inlay and the brass holder) in the operating mode.

components are mixed in the pre-mixing chamber (~ 1 nl volume) at the Reynolds numbers $Re \sim 500-1000$, the sample-mixing time is $\tau_m = 18$ μs at 3.4 ml min^{-1} flow rate. On the other hand, if the mixing occurs in the orifice (~ 10 pl volume), the sample-mixing time at the same flow rate is much shorter, $\tau_m \sim 180$ ns, and the Reynolds number is higher, $Re \sim 4000$.

We have sufficient data showing that the mixing of the reaction components does not occur in the pre-mixing chamber, and the τ_m values are confined to the (sub)microsecond domain according to the calculations above. Detailed studies on the mixer characterization and determination of the mixing time are to be published as a separate paper elsewhere.

2.4.2. Mixing efficiency

The efficiency of mixing has been assayed by measuring the extent of a diffusion-limited reaction as a function of the solution viscosity. The protonation of 2-hydroxycinnamic acid (2-HCA) has been used for this purpose. In general, the rate constant of proton transfer ranges between ~ 10^8 and 10^{11} M^{-1} s^{-1}, and for a small organic molecule such as 2-HCA it is around 5×10^{10} M^{-1} s^{-1} [3]. In the case of 2-HCA, the protonation is accompanied by a characteristic quenching of the fluorescence emission at 493 nm, so the extent of the reaction can be monitored accordingly (Fig. 5). To vary the viscosity, glycerol was added to the 2-HCA solution in increasing amounts, and the mixing with HCl was assayed as described in Experimental procedures. The results are shown in Fig. 6. The mixing efficiency is ~ 100% at 0–35% glycerol, decreasing to ~ 50% at 60% glycerol. The viscosity values that correspond to the glycerol concentrations used are shown on the second top axis of Fig. 6. On the top axis, the "protein concentration" values are displayed that correspond to the viscosity of the solution. The former were estimated using Einstein's basic analysis of the dependence of the relative viscosity on the concentration of rigid spherical particles [169,170], extended to suspensions of high particle concentrations [171], and further adapted for protein solutions [172,173] (Eq. (3)).

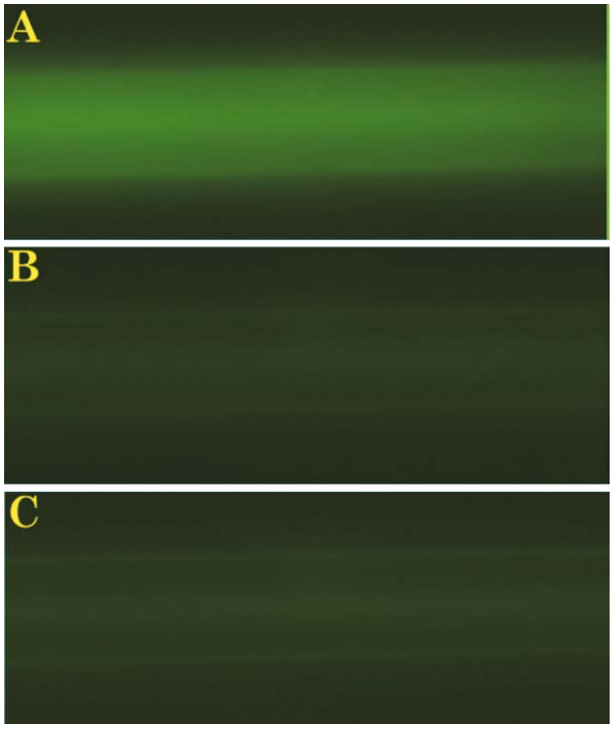

Fig. 5. Two-component liquid mixing in the novel tangential micromixer: quenching of the 2-HCA-fluorescence emission by HCl. 0.2 mM 2-HCA, pH = 9.2 was mixed with 10 mM HCl to induce a pH-jump and protonate 2-HCA. Images of the jet were taken ~ 0.8–1 mm away from the orifice of the micro-mixer (at 4–5 μs after mixing). (A) Fluorescence emission of the 0.2 mM 2-HCA mixed with water. (B) Quenching of the fluorescence emission of 2-HCA after mixing with HCl. (C) Dark count: fluorescence emission of water recorded under conditions identical to above. The jet was visualized as described in Experimental procedures.

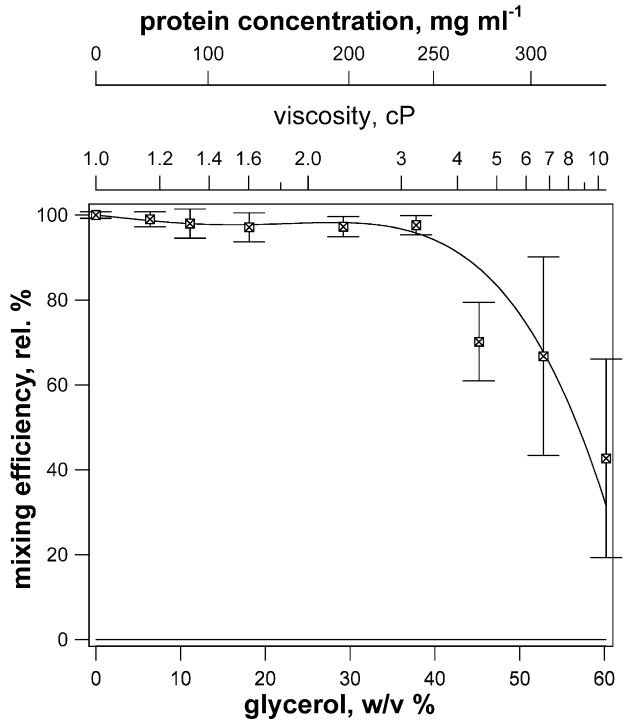

Fig. 6. Efficiency of mixing in the novel tangential micro-mixer as function of the solution viscosity of the reaction component (2-HCA). The efficiency of mixing was calculated from multiple series of the fluorescence emission images (similar to the images shown in Fig. 5) as described in Experimental procedures. The second top axis (solution viscosity) was calculated from the glycerol content using Eq. (3) with the empiric coefficients $A = 2.29 \times 10^{-2}$, and $B = 6.94 \times 10^{-3}$. The top axis showing the protein concentration was calculated from the solution viscosity values taking $A = 2.718 \times 10^{-3}$ m^3 kg^{-1}, and $B = 1.842 \times 10^{-3}$ m^3 kg^{-1}, as determined for lysozyme at 35 °C in Ref. [172].

$$\eta_r = \exp\left(\frac{Ac}{1 - Bc}\right) \quad (3)$$

η_r is the relative viscosity $\eta_r = \eta/\eta_o$; η and η_o denote the viscosity of the solution and the solvent, respectively, c is

the protein concentration; A, B are the empiric coefficients experimentally determined for concentrated lysozyme solutions at 35 °C, $A = 2.718 \times 10^{-3}$ mg^{-1} ml, and $B = 1.842 \times 10^{-3}$ mg^{-1} ml.

From Fig. 6 it follows that the micro-mixer is capable of efficient mixing of protein samples with concentrations up to 250 mg ml^{-1}. For lysozyme (chicken egg-white, $M_w \sim 14.3$) this corresponds to ~ 18 mM protein. Thus, the novel micro-mixer can be considered as an excellent tool for the preparation of pre-steady samples for detailed spectroscopic structure analyses, which require concentrated protein samples (~ 1 mM).

2.5. Model system to determine the minimal sample-ageing time

The binding of azide (N_3^{1-}) to metmyoglobin from horse heart ($MbFe^{3+}$) was used as a molecular timer to characterize the mixing and freeze-quenching properties of the novel setup. This choice of the reaction system allowed us to analyze freeze-quench samples using low-temperature optical absorbance spectroscopy and X-band EPR spectroscopy. In retrospect, the disadvantages of the reaction couple $MbFe^{3+}$–N_3^{1-} are (a) the unexpectedly slow kinetics at high azide concentrations, and (b) the complex binding mechanism, both phenomena not noticed before [174–177] because the time scale of these studies was in the millisecond time domain.

The binding rate of azide is known to increase at low pH Fig. 7, lower graph, Table 2) [178]. On the other hand, metmyoglobin tends to (partially) precipitate at pH < 5 within minutes of storage. For our analysis we chose the pH = 5.0, when metmyoglobin is stable in solution for hours (not shown).

To characterize the reaction between $MbFe^{3+}$ and N_3^{1-}, we performed a pre-steady state kinetic analysis in a stopped-flow instrument. Analysis of the kinetic traces recorded at different azide concentrations displayed an unusual, two-rate-constant kinetic behavior (Fig. 7) that resembles the kinetic data obtained for the ferric haemoproteins from other sources [179]. The second-order rate constant for azide binding calculated from observed relaxation times at different azide concentrations is roughly 10-fold higher at $[N_3^{1-}] < 1$ mM than at $[N_3^{1-}] > 10$ mM. The rate constants are only weakly dependent on the ionic strength of the solution, in agreement with previously reported data [178]; addition of 0.8 M NaCl leads to a decrease of the binding rates at both "high" and "low" $[N_3^{1-}]$ of < 20% (not shown). The ratio between the k_{obs} values at "low" and "high" $[N_3^{1-}]$ is pH-dependent: it is the highest at low pH ($k_{obs}^{low}/k_{obs}^{high} \sim 16$ at pH = 4, see Table 2), while, at pH ~ 7 it approaches unity: the binding becomes essentially "monophasic" [174,175,177].

In our opinion, and in agreement with similar proposals availing in the literature [179–183], the reaction between

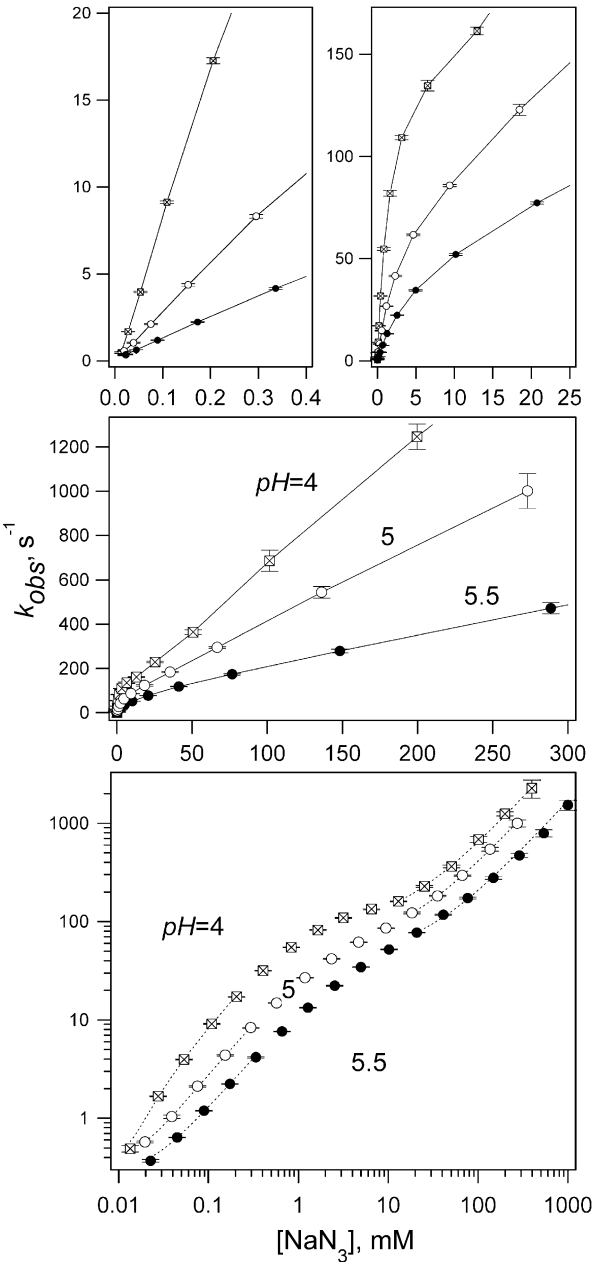

Fig. 7. "Biphasic kinetics" of metmyoglobin–azide binding reaction: the $[N_3^{1-}]$-dependent change of the observed rate constant values. The binding reaction was studied in the stopped-flow instrument at 5 °C. Horse heart metmyoglobin was mixed with sodium azide solution resulting in 11 μM $MbFe^{3+}$, and 13.41 μM, 27.53, 53.39, 108.7, 205.3, 406.3, 836.4 μM, 1.653 mM, 3.173, 6.52, 12.95, 25.38, 50.76, 101.63, 199.56, and 395.69 mM N_3^{1-} at pH = 4 (crossed squares); 19.63 μM, 39.07, 75.39, 153.54, 295.43, 573.5 μM, 1.19 mM, 2.343, 4.703, 9.417, 18.48, 35.36, 66.82, 136.25, and 273.2 mM N_3^{1-} at pH = 5 (open circles); 22.72 μM, 44.71, 89.02, 172.9, 336.1, 658.4 μM, 1.276 mM, 2.547, 4.964, 10.19, 20.73, 41.09, 76.65, 148.2, 288.6, 538,6 mM and 1 M N_3^{1-} at pH = 5.5 (closed circles). Prior to the stopped-flow shots at pH = 5 and 5.5, both metmyoglobin and azide were pre-equilibrated to the appropriate pH in 25 mM Na-citrate buffer. At pH = 4, metmyoglobin was dissolved in water, and mixed with the pH-pre-equilibrated azide, triggering both pH-jump and binding of azide to the protein. The values of the observed rate constant were determined by fitting the exponential fitting function to the stopped-flow traces. The dotted traces on the lower graph were computed by fitting Eq. (5) to the experimental data.

metmyoglobin and azide proceeds according to the following reaction scheme.

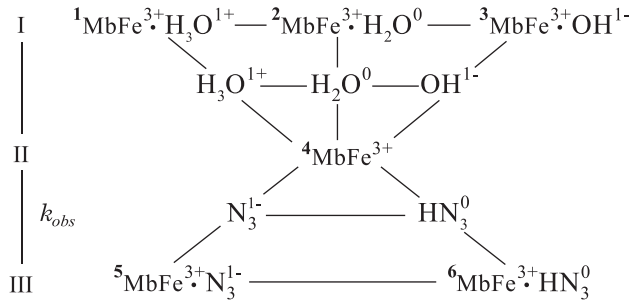

The binding of azide occurs as a displacement of the water/hydroxyl/hydroxonium molecule at the hexacoordinated heme iron. The binding reactions (**4–5**, **4–6**) are proposed to occur under the conditions when $d[^4MbFe^{3+}]/dt \sim 0$, because the equilibration between water and myoglobin is faster than the subsequent binding of a ligand [184]. Based on simple electrostatics, one would expect that the rates of water-myoglobin equilibration increase in the sequence **3–4** < **2–4** < **1–4**. The slowest is the dissociation of OH^{1-}, followed by the dissociation of H_2O; the dissociation of the hydroxonium ion H_3O^{1+}, supposedly, is the fastest process ($\gg 10^4\ s^{-1}$). The water-myoglobin equilibrium is pH-dependent too. With decreasing pH, the equilibrium shifts towards the free $^4MbFe^{3+}$ due to the formation of an unstable $^1MbFe^{3+}\cdot H_3O^{1+}$. At alkaline pH the equilibrium shifts towards the water-bound species $^2MbFe^{3+}\cdot H_2O^0$ and $^3MbFe^{3+}\cdot OH^{1-}$. As a result, the concentration of $^4MbFe^{3+}$ is higher at low pH, leading to an apparent increase of the azide-binding rate.

At pH = 5 and azide concentrations below 1 mM, the water-myoglobin equilibration via the routes **1–4** and **2–4** occurs faster than the binding of azide (routes **4–5** and **4–6**). At $[N_3^{1-}]$>10 mM, the rate of binding of azide exceeds the rate of dissociation of water from the heme iron (route **2–4**); on the other hand, it is still significantly slower than the dissociation of $^1MbFe^{3+}\cdot H_3O^{1+}$ via the route **1–4**. This shift of the dynamic equilibrium leads to an approximately 10-fold decrease of the $^4MbFe^{3+}$ concentration, causing a ~ 10-fold decrease of the apparent binding rate constant (k^{app}).

The detailed elucidation and verification of this mechanism, however, falls beyond the scope of this paper. For the purpose of using the myoglobin–azide couple as a molecular timer, a semi-empirical treatment of the reaction mechanism was found sufficient. At $[N_3^{1-}] \notin [1,10]$ mM, the reaction is essentially "monophasic" and can be adequately treated as an associative bimolecular collision,

$$MbFe^{3+} + N_3^{1-} \underset{k_{-1}^{app}}{\overset{k_1^{app}}{\Leftrightarrow}} MbFe^{3+}\cdot N_3^{1-}$$

The integration of the corresponding differential equation yields thefollowing analytical solution.

$$C(t) = \alpha\frac{1 - e^{k_1^{app}\gamma t}}{1 - \beta e^{k_1^{app}\gamma t}},$$

where

$$\gamma = \sqrt{([Mb]_0 + [N_3]_0 + K_d^{app})^2 - 4[Mb]_0 + [N_3]_0},$$

$$\alpha = \frac{2[Mb]_0 + [N_3]_0}{[Mb]_0 + [N_3]_0 + K_d^{app} + \gamma},$$

$$\beta = \frac{[Mb]_0 + [N_3]_0 + K_d^{app} - \gamma}{[Mb]_0 + [N_3]_0 + K_d^{app} + \gamma}, \text{and } K_d^{app} = \frac{K_{-1}^{app}}{K_1^{app}},$$

$[Mb]_0$, and $[N_3]_0$ are the initial concentrations of metmyoglobin and azide, respectively.

Under the pseudo-first order approximation, $[N_3]_0 \gg [Mb]_0$, K_d^{app}, the parameters approach $\gamma \to [N_3]_0$, $\alpha \to [Mb]_0$, $\beta \to 0$, and the solution reduces to

$$C(t) = [Mb]_0(1 - e^{-k_{obs}t}) \quad (4)$$

where

$$k_{obs} = k_1^{app}\gamma \quad (5)$$

$$k_{-1}^{app} = \kappa\frac{ekT}{h}e^{\frac{\Delta S_{-1}^{\#}}{R}}e^{-\frac{E_A^{-1}}{RT}} \quad (6)$$

and

$$K_d^{app} = e^{\frac{\Delta S_{-1}^{\#} - \Delta S_1^{\#}}{R}}e^{\frac{E_A^1 - E_A^{-1}}{RT}}, \quad (7)$$

the transmission coefficient $\kappa = 1$.

In principle, Eq. (5) can be further simplified to $k_{obs} = k_1^{app}[N_3]_0 + k_{-1}^{app}$.

Fitting of Eq. (5) to the experimental data is shown in Figs. 7 and 8 (dotted traces). It follows the k_{obs} values closely when $[N_3^{1-}] \notin [1,10]$ mM.

To complete the empirical characterization, the binding of azide was assayed at different temperatures, and the kinetic and thermodynamic parameters were determined at both low (< 1 mM), and high (>10 mM) $[N_3^{1-}]$, in the wide range of azide concentrations (20 μM–1.5 M) (Fig. 8A–C). The values are summarized in Table 3. Using these values, one can calculate the binding rate at any temperature and azide concentration (at pH = 5), which appears to be sufficient for the determination of the sample-ageing time of the MHQ instrument.

2.6. Multi-wavelength analysis and deconvolution of two-component spectra

In the present work, the extent of binding of azide (N_3^{1-}) to metmyoglobin from horse heart ($MbFe^{3+}$) was determined using both low-temperature optical absorbance spectroscopy and X-band EPR. Each freeze-quenched sample

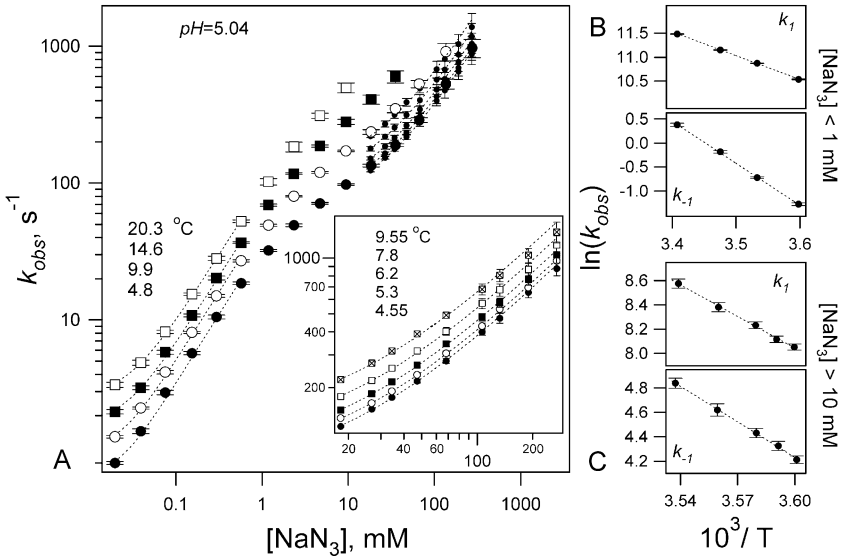

Fig. 8. Temperature-dependence of the kinetic parameters for the azide-metmyoglobin binding reaction determined at pH = 5. A. Variation of the observed rate constant with $[N_3^{1-}]$ measured at different temperatures. Inset: blow-up of the binding data at high azide concentrations. The dotted traces were computed by fitting Eq. (5) to the experimental data. (B, C) Arrhenius plots for the k_1 and k_{-1} apparent rate constants determined at $[NaN_3] < 1$ mM (B), and $[NaN_3] > 10$ mM (C). The k_1^{app} and k_{-1}^{app} values were calculated using Eq. (5). The binding reaction was studied in the stopped-flow instrument at pH = 5.04. Horse heart metmyoglobin was mixed with the sodium azide solution, resulting in 11 μM $MbFe^{3+}$, and 19.63 μM, 39.07, 75.39, 153.54, 295.43, 573.5 μM, 1.19 mM, 2.343, 4.703, 9.417, 18.17, 18.48, 26.82, 34.52, 35.36, 47.35, 66.82, 67.98, 106.28, 132.76, 136.25, 189.88, 270.7, and 273.2 mM N_3^{1-}. The values of the observed rate constant were determined by fitting the exponential fitting function to the stopped-flow traces.

contains a mixture of non-reacted $MbFe^{3+}$ and the reacted complex $MbFe^{3+}{\cdot}N_3^{1-}$. The corresponding spectra thus represent a superposition of the electronic absorbances of these compounds, or their first derivatives in case of EPR. In each case, the fraction of conversion, or the relative ratio of $[MbFe^{3+}{\cdot}N_3^{1-}]$ to the total concentration of metmyoglobin species, $[MbFe^{3+}]_0$, depends on the sample-ageing time, reaction temperature, and $[N_3^{1-}]$.

The aim of the procedure below is to deconvolute the mixed spectra of the freeze-quenched samples into the individual spectral components, and to determine the fraction of conversion in each case. Deconvolution is confronted by experimental complications arising during the sample preparation and recording the spectra, as mentioned below. (i) Sample-to-sample variation of the effective chromophore concentration (EfC) in the cuvette due to the packing-dilution uncertainty (up to 20–30%). (ii) Sample-to-sample variation of the baseline slope and absorbance offset for the independently prepared otherwise identical samples. (iii) Slightly different spectral characteristics of metmyoglobin samples prepared by ''slow''* freezing of aqueous solutions with respect to ''rapidly'' freeze-quenched samples. (*) Slow freezing was carried out by pipetting 1 ml of sample solution to the cuvette pre-cooled to 77K).

For the metmyoglobin–azide reaction couple, the first two points relate to both optical absorbance spectroscopy and X-band EPR, while the last point appeared relevant for optical spectroscopy only.

The reason for the variation of the slope and the offset of the baseline in the optical absorbance spectra might stem from the inhomogeneity and/or different microstructure of the isopentane matrix under (a) slightly different freezing conditions, (b) different packing concentrations of the ice-sample suspension, and (c) spectrum-to-spectrum variation of the temperature drift (80–110 K) in the low-temperature setup during scan averaging. For the analysis we assumed that these effects yield proportional/linear baseline shifts between 460 and 710 nm. The following procedure has been found to give satisfactory deconvolution results.

(1) Electronic absorbance spectra of the freeze-quenched samples (Fig. 9A) were baseline-corrected by fitting with a linear regression in the case of optical absorbance spectroscopy, or with a weighted high-term polynomial fitting in the case of EPR (see Experimental procedures). The residuals of the fitting were taken for further analysis as the baseline-corrected spectra (Fig. 9B).

(2) *Relative* spectral extinctions of the individual components, $MbFe^{3+}$ and $MbFe^{3+}{\cdot}N_3^{1-}$, were determined. For that, pure (one-component) spectra, S_P and S_S, were recorded *at the same EfC*. (S_P is the spectrum of the product, $MbFe^{3+}{\cdot}N_3^1$; S_S is the spectrum of the starting material, $MbFe^{3+}$). In the case of optical absorbance spectroscopy, a large number of freeze-quench samples of $MbFe^{3+}$ and $MbFe^{3+}{\cdot}N_3^{1-}$ (~ 50 each) were prepared starting with the same amount of protein. The recorded spectra were corrected for the baseline and averaged to minimize the uncertainty of packing dilution. ''Slowly'' frozen metmyoglobin samples could

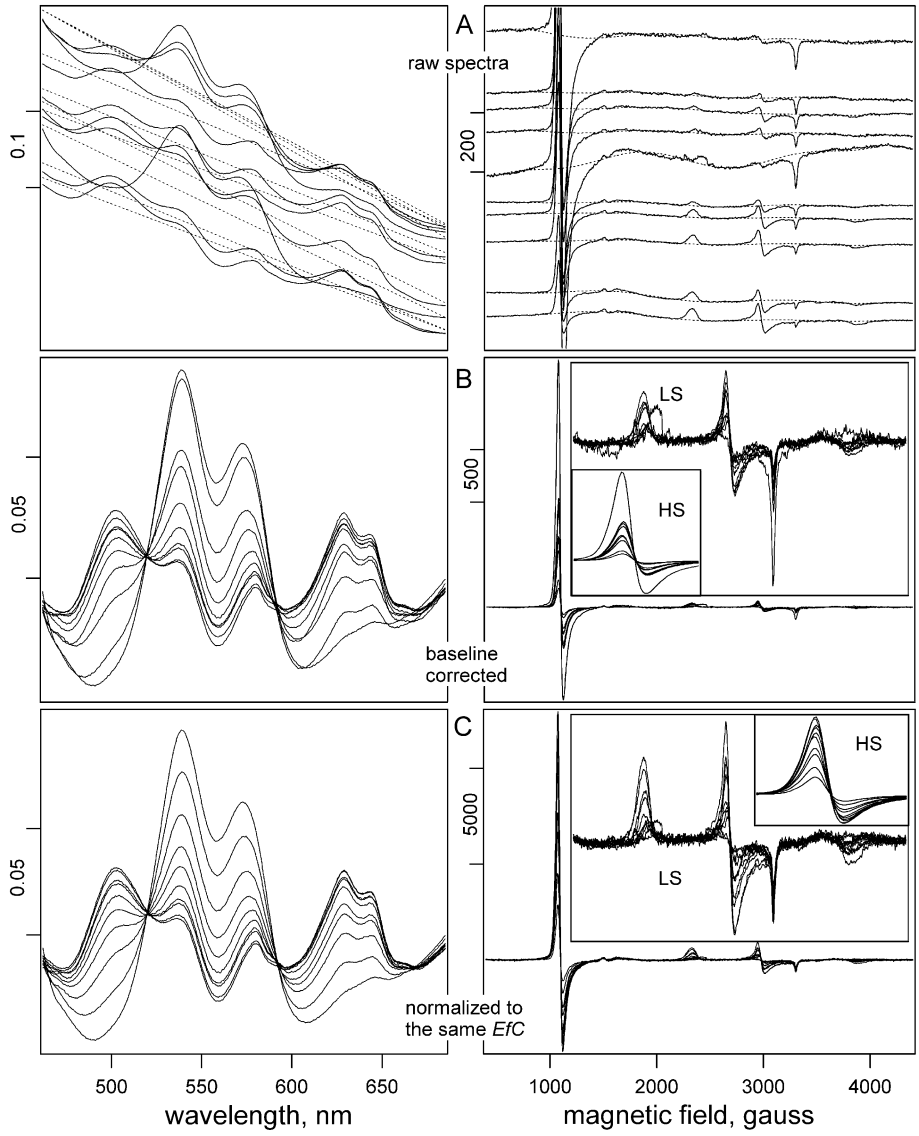

Fig. 9. Processing of the spectral data. Optical absorbance spectroscopy at 77K (left), and X-band EPR at 18K (right). (A) Raw spectra. Samples were obtained at different concentrations of sodium azide and at a distance to the cryomedium surface of 6.2 cm. The sample volumetric flow rate was 2.0 ml min^{-1} (~ 117 m s^{-1}). Final concentrations are [$MbFe^{3+}$]—0.73 mM; [NaN_3]—4.24 mM, 8.01, 15.62, 31.45, 64.99, 131.1, 243.97, 464.24, 898.58 mM, and 1.415 M, pH = 5. Dotted traces are calculated by fitting a linear regression (left), or a weighted high-term polynomial function (right) to the recorded spectra. The fitting residuals were used as the "baseline-corrected" spectra shown in (B). Insets show the blow-up of the high-, or low-spin regions of the spectrum. Eq. (8) was fitted to the "baseline-corrected" spectra in (B); in each case the "dilution coefficient" of the spectrum was calculated with respect to the spectra of pure compounds S_S and S_P. The spectra in (C) were normalized to the same EfC by dividing the spectra in (B) by the "dilution coefficient". The weighted fitting with a polynomial function is described in Experimental procedures.

not be used as a reference for deconvolution because their spectral characteristics differ from the "rapidly" frozen samples in band positions by 2–4 nm and relative band intensities for 4–6%. In the case of X-band EPR, the spectra of the "slow" and "fast" frozen samples were found essentially identical.

(3) Baseline- and EfC-normalized spectra of the individual components obtained above, S_P and S_S, were used further for the deconvolution of the mixed spectra $MbFe^{3+}$–$MbFe^{3+}{\cdot}N_3^{1-}$. Given the fact that the total concentration of metmyoglobin remains constant during the reaction, the multivariate function was fitted to each mixed spectrum as follows.

$$^{Fit}S_X = D(S_S(1-C) + CS_P) \quad (8)$$

$^{Fit}S_X$ is the fit of the mixed spectrum S_X; S_S is the spectrum of $MbFe^{3+}$ (first variable); S_P is the spectrum of $MbFe^{3+}{\cdot}N_3^{1-}$ (2nd variable); D is the fitting parameter—the

"packing-dilution coefficient"—the dilution of S_X with respect to S_S and S_P; C is the fitting parameter—the fraction of conversion for the sample S_X. The percentage of conversion $C_{\%} = 100\ C$.

Extraction of the "packing-dilution coefficient" allowed us to normalize all mixed spectra to the same EfC value. The time-resolved spectra of the reaction between $MbFe^{3+}$ and N_3^{1-}, corrected for the baseline and normalized for the "packing-dilution", are shown in Fig. 9C.

Analyses of the fitted spectra, ${}^{Fit}S_X$, yield additional important information about the formation of transient intermediates in the reaction. In the case of two-component conversion $S_S \rightarrow S_P$, the fitting residuals of the mixed spectrum S_X are expected to converge to the instrument noise. Appearance of the residuals with repeatable patterns where the signal intensities are dependent on the sample-ageing time and/or on the concentrations of the reaction components would indicate the presence of reaction intermediate(s). Even in the case of a seemingly simple reaction, such as metmyoglobin–azide binding, we have been able to observe a spectral signature of a transient intermediate (see below).

In summary, the advantages of the global spectrum analysis described above are as follows.

(1) It is not necessary to know *the effective concentration* of the absorbing species in the cuvette to deconvolute the mixed spectrum; *the relative spectral ratio* of the individual components suffices.
(2) Every data point in the spectrum contributes to the determination of the percent of conversion and the packing dilution of the sample.
(3) Analysis of the fitting residuals in Eq. (8) yields information on the presence of reaction intermediates.

2.7. Estimation of the reaction temperature

The rate of the molecular timer (binding of azide to HH metmyoglobin) that was used for the determination of the freeze-quenching time depends on several important parameters, such as ionic strength, pH and the reaction temperature. A chemical reaction in a thermodynamically opened system (i.e. a free-flowing jet at low pressure) differs from the reaction in a closed vessel, because the isothermal approximation is no longer applicable. Direct measurements of the jet temperature showed that the latter is dependent on the pressure in the low-pressure chamber, roughly decreasing for ~ 0.5 deg/100 mbar; some distance-dependence has been observed, ~ 0.5 deg cm^{-1}. In addition, the temperature of the jet drops by ~ 3–5 °C in the vicinity of the isopentane surface (<5 cm).

The following reasons for the temperature drop can be envisaged: (a) degassing of the jet, (b) adiabatic expansion of the dissolved gases (c) evaporation of water from the jet surface, and (d) cooling of the jet by the vapors of cryomedium.

To estimate the actual reaction temperature, the binding of myoglobin and azide was performed at fixed concentrations of both components. In this experiment, we varied the freeze-quenching time, and, consequently, the degree of conversion by changing the jet speed and the distance between the mixer and the cryomedium surface. To transform the speed-distance into reaction-time coordinates, the following assumptions have been made: (a) the mixing time was taken as the total residence time of the sample in the mixer (determined from volumetric flow rate and mixer dimensions); (b) the jet speed was taken 10% higher than estimated from the volumetric flow rate and orifice diameter, based on direct measurements of the jet speed using Laser Doppler Anemometry (LDA); (c) based on previous experimental [148] and numerical studies [149,150], the sample cooling rate in isopentane was assumed to be 3×10^6 deg s^{-1}.

The variation in distance and jet speed results in variation of the reaction times for nearly two orders of magnitude, so that the overall duration of the binding reaction is well covered (Fig. 10).

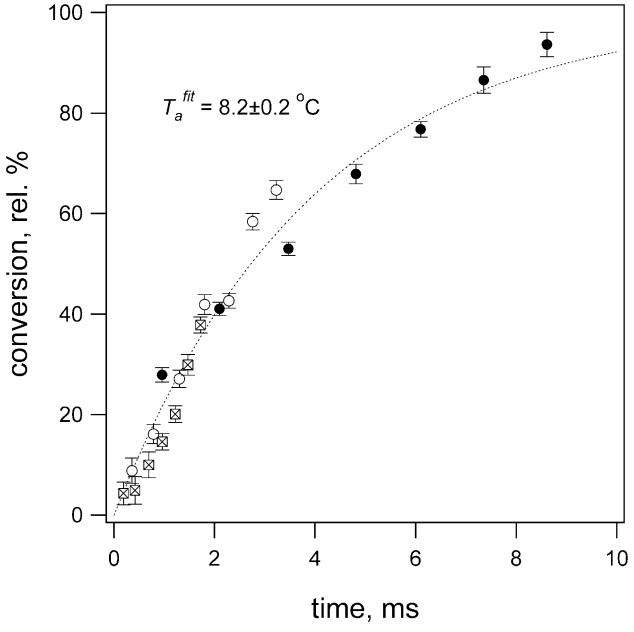

Fig. 10. Integrated (time-resolved) product formation trace for the metmyoglobin–azide binding reaction. The percent of conversion was calculated by fitting Eq. (8) to the individual spectra (shown in the insert). The time values on the bottom axis were calculated as described in the text. Metmyoglobin was mixed with sodium azide at pH = 5 (final concentrations $[MbFe^{3+}] = 0.73$ mM, $[NaN_3] = 33.29$ mM). Solid circles—data obtained at a volumetric flow rate of 0.6 ml min^{-1} (~ 35 m s^{-1}), and at distances to the cryomedium surface of 3, 7, 11.8, 16.5, 21, 25.4, and 29.8 cm. Empty circles—1.6 ml min^{-1} (~ 93 m s^{-1}), the same distances. Crossed squares—3 ml min^{-1} (~ 175 m s^{-1}), the same distances. The dotted trace was calculated by fitting Eqs. (4)–(7) to the integrated data, using the reaction temperature as the parameter (fitted value T_a^{fit} is shown).

To extract the T_a^{fit} (average* reaction temperature) value, the analytic solution of the reaction mechanism (4) was rewritten in its thermodynamic form via $\Delta S^{\#}$, E_A (Eqs. (6) and (7)), and fitted to the experimental data points. (*Average relates here to the fact that the temperature of the jet is taken constant along the jet length, and the time/distance-dependent temperature gradient, as well as the jet speed-dependent variation of the freeze-quenching time are neglected.) The $\Delta S^{\#}$, E_A values were taken from Table 3.

It follows from the fitting that the average temperature of the jet decreases from 20 to ~ 8.2 °C at a pressure of ~ 150 mbar (Fig. 10).

2.8. Determination of the sample-ageing time

Knowing the value of the average reaction temperature, we set out to determine the sample-ageing times at several different flow rates and jet lengths by varying the azide concentration. Five different sets of values of the jet speed and the jet length were chosen to demonstrate the dynamic range of the MHQ instrument in the microsecond time domain. For determination of the instrument "dead-time" the maximal jet speed was 187 m s^{-1}, which is very close to the maximum attainable with the HPLC pumps with the backpressure limit of 400 bar. The minimal jet length was ~ 20 mm. The calculated sample-ageing time for this jet speed/length combination is τ_a^{calc} ~ 134 μs. For the reaction time of τ_a^{calc} ~ 2.4 ms, the jet length was taken as ~ 28 cm and the speed was 117 m s^{-1}. The other three sets had intermediate values, yielding the sample-ageing times between 134 μs and 2.4 ms.

For each τ_a^{calc} value, the optical absorbance spectra of metmyoglobin/azide mixtures obtained at different azide concentrations are shown in Fig. 11A–D. All spectra were corrected for the baseline offset, and normalized for the packing dilution. In the lower graph the sample-to-sample variations of EfC values with respect to the pure spectra S_S and S_P are shown. S_S and S_P are also included in the top graphs in each series of the spectra. It can be seen that the degree of conversion at a given τ_a^{calc} value increases with increasing of azide concentration in the reaction mixture, and the exponential $[N_3^{1-}]$-dependent product formation curves similar to the time-dependent curve shown in Fig. 10 can be constructed (Fig. 12). For each data point of the curve, the percent of conversion was calculated by fitting the Eq. (8) to the mixed spectra of the relevant MHQ sample; the fitting residuals are shown below each series of spectra in Fig. 11. At long reaction times (as in C and D) and high $[N_3^{1-}]$, the residuals show a consistent deviation from linearity around 580–582 nm, indicating a red shift of the α-band of the low spin $MbFe^{3+}{\cdot}N_3^{1-}$ complex. The reason might stem from denaturation/precipitation of metmyoglobin at low pH and high azide concentrations [178], a process that is too slow to interfere with the binding reaction between 0.1 and 0.5 ms, but is apparent on the 0.5–2.5-ms time scale.

Fig. 12 illustrates the time-resolving power of the modern pre-steady state mixing-and-sampling techniques, such as stopped-flow/freeze-quench and MHQ. The dynamic range of the stopped-flow/freeze-quench covers the seconds-to-milliseconds time scale, while MHQ takes it over from milliseconds to microseconds.

To plot the stopped-flow and MHQ data on the same format, the stopped-flow traces are shown as the $[N_3^{1-}]$-dependent product formation curves recorded at a fixed reaction time. For that, time-dependent absorbance traces were acquired in the stopped-flow instrument at 16 different azide concentrations. Eight values of the reaction times were chosen, ranging between τ_a^{calc} = 2.7 s and τ_a^{calc} = 8 ms, and the percent of conversion was calculated for each trace at each reaction time. For each τ_a^{calc} value, the calculated values of percent of conversion were plotted versus the azide concentration (Fig. 12, traces 1–8, open circles). The stopped-flow experiments were performed at 4.8 °C as described in Experimental procedures.

MHQ traces obtained at fixed jet speed (~ 117 m s^{-1}) and different jet lengths (2–29 cm) are shown with solid circles (traces 9–13). Trace 13 was obtained at the maximal flow rate of 3.2 ml min^{-1} (187 m s^{-1}) and the minimal distance of 20 mm yielding the shortest reaction time.

Each trace in Fig. 12 corresponds to a different τ_a^{calc} value. From left to right of the graph, the sample-ageing times span the range from 2.7 s at low azide concentrations (0.02–1 mM, trace 1) to 2.4 ms in the middle (1–100 mM, trace 9), and to 134 μs at high azide concentrations (100 mM–2 M, trace 13).

To extract the fitted values of the sample-ageing time, τ_a^{fit}, the following equation was fitted to the experimental data in Fig. 12.

$$^{Fit}C_p = A + Be^{-k_{obs}^{High}\tau_a^{fit}} + Ce^{-k_{obs}^{Low}\tau_a^{fit}} \quad (9)$$

k_{obs}^{Low} is the observed rate constant as in Eqs. (4)–(6) at $[N_3^{1-}]$ < 1 mM and 8.2 °C, k_{obs}^{High}—ibid. at $[N_3^{1-}]$ >10 mM; A, B, C, and τ_a^{fit} are the fitting parameters. Using this equation we assume that at a given reaction time the binding of azide to metmyoglobin is a sum of two parallel and independent reactions, i.e. one with a high rate-constant, designating binding at "low" $[N_3^{1-}]$ (< 1 mM), and one with a low-rate-constant binding at "high" $[N_3^{1-}]$ (>10 mM), with the rate constants summarized in Table 3.

The fitted τ_a^{fit} values are shown in Table 4. For the stopped-flow data the τ_a^{calc} values were determined (Tables 2 and 3) and serve as a control for the validity of the "biphasic" fitting assumption (9). It can be seen that the deviation between the fitted and calculated values is small, falling within 4–7% of the τ_a^{calc} value. In the "transition" range of azide concentrations, between 1 and 10 mM, the deviation increases to 20% (Fig. 12, traces 6–10, Table 4).

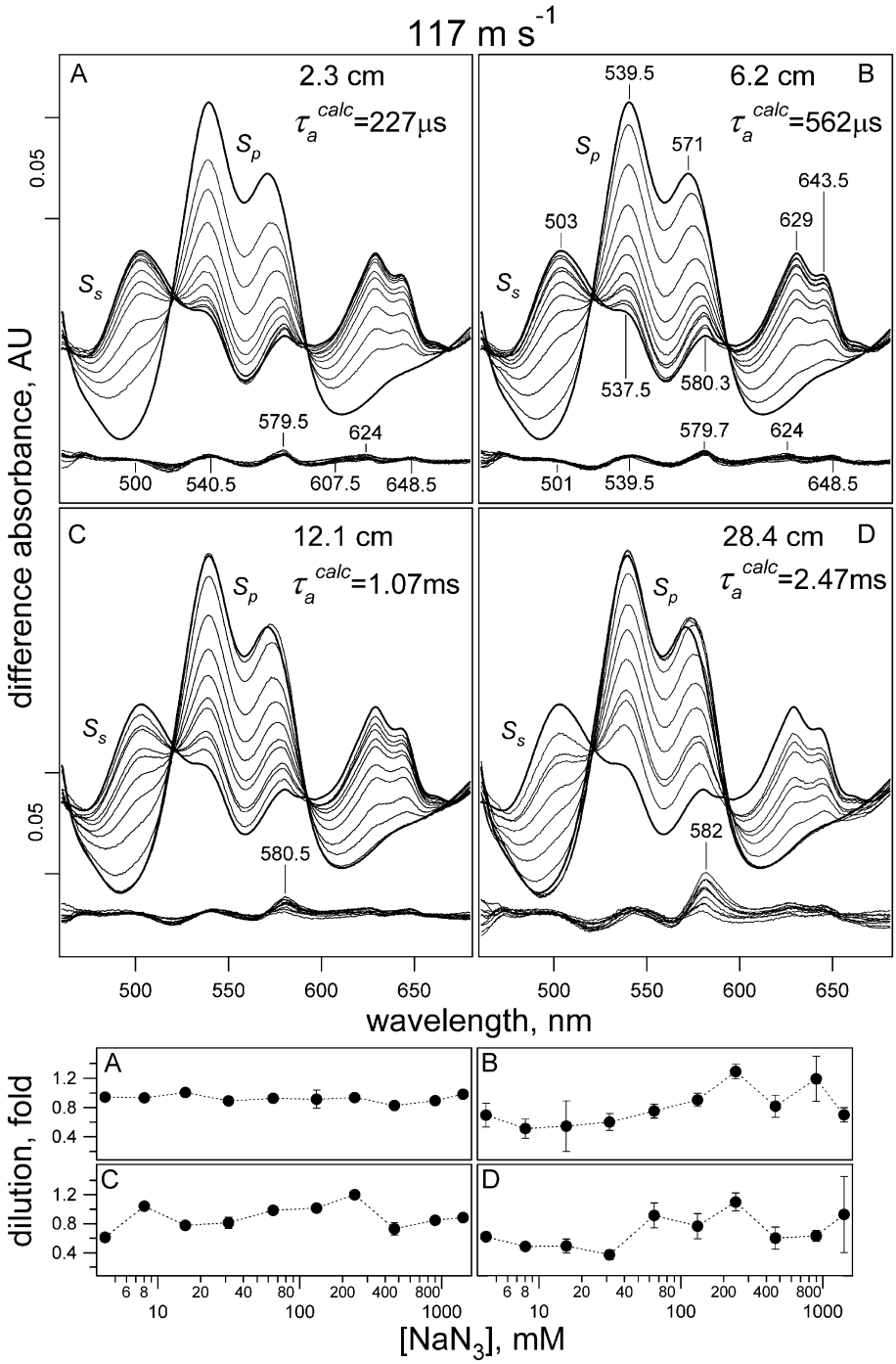

Fig. 11. Baseline-corrected and EfC-normalized 77K optical absorbance spectra of the metmyoglobin–azide MHQ samples. Samples were obtained at different concentrations of sodium azide and distances to the cryomedium surface. The sample volumetric flow rate was 2.0 ml min^{-1} (~ 117 m s^{-1}). (A) Samples were sprayed in the cryomedium from a distance of 2.3 cm. Final concentrations are [$MbFe^{3+}$]—0.73 mM; [NaN_3]—4.24 mM, 8.01, 15.62, 31.45, 64.99, 131.1, 243.97, 464.24, 898.58 mM, and 1.415 M, pH = 5. (B) The distance is 6.2 cm. (C) 12.1 cm. (D) 28.4 cm. Eq. (8) was fitted to each reaction mixture spectrum, employing the spectra of the pure compounds $MbFe^{3+}$ (S_S) and $MbFe^{3+}{\cdot}N_3^-$ (S_P) as the independent fitting variables (spectra are shown in the graphs). The "dilution coefficient" fitting parameter D is shown in the four lower graphs. The [NaN_3]-resolved product formation curves calculated from the "percent of conversion" $C_{\%}$ (see Eq. (8)) are shown in Fig. 12. The residuals of the fitting are shown below each series of the spectra.

At these concentrations, the binding rates with a high and a low rate constant are of the same order of magnitude, and the difference between the exponential coefficients of the double exponential fitting function (Eq. (9)) is small. This generally causes the least-square fitting algorithms to give a higher uncertainty for fitting parameters.

In parallel to the low-temperature optical absorbance spectroscopy, a series of MHQ samples has been analyzed

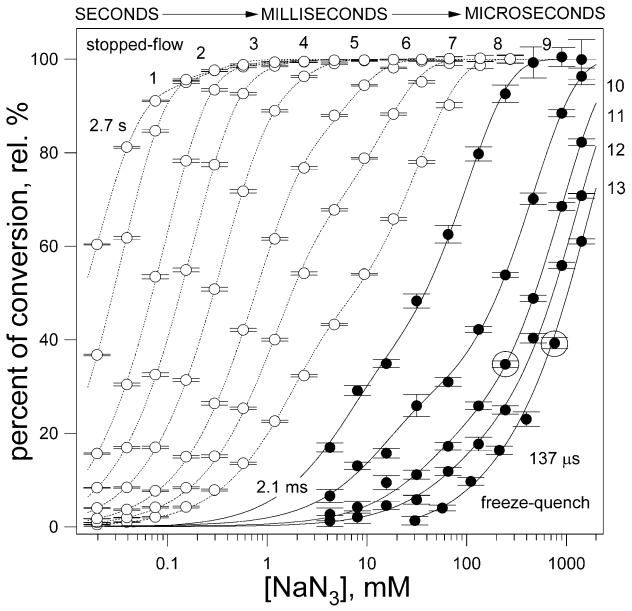

Fig. 12. [NaN_3]-resolved product formation curves for the metmyoglobin–azide binding reaction. Open circles (traces 1–8)—data obtained from the stopped-flow experiments. Closed circles (traces 9–13)—data obtained from the MHQ experiments. Dotted/solid traces are obtained by fitting Eq. (9) to the data values, using the sample-ageing time as the fitting parameter (fitted values are shown in Table 4). The sample-ageing times for traces 1–13 span from 2.3 s to 137 µs. The conversion of the stopped-flow traces (absorbance vs. time)-format to the (percent of conversion vs. [NaN_3])-format was performed using Eqs. (4)–(7) as mentioned in the text. The conditions for preparation of MHQ samples were as follows. Trace 9 (τ_a^{calc} ~ 2.47 ms)—see Fig. 11D; trace 10 (1.07 ms)—Fig. 11C; trace 11 (562 µs)—Fig. 11B; trace 12 (227 µs)—Fig. 11A; trace 13 (134 µs)—Fig. 16A. Spectra corresponding to the encircled data points are shown in Fig. 16B.

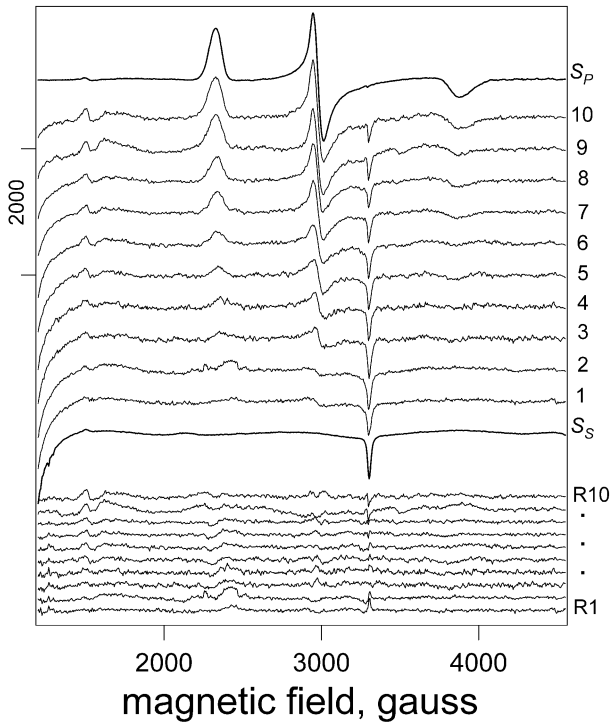

Fig. 13. Baseline-corrected and EfC-normalized X-band EPR spectra of the metmyoglobin–azide MHQ samples. Samples were obtained at different concentrations of sodium azide and distance to the cryomedium surface of 6.2 cm. The sample volumetric flow rate was 2.0 ml min^{-1} (~ 117 m s^{-1}). Final concentrations are [$MbFe^{3+}$]—0.73 mM; [NaN3]—4.24 mM, 8.01, 15.62, 31.45, 64.99, 131.1, 243.97, 464.24, 898.58 mM, and 1.415 M, pH = 5, with the spectrum 1 corresponding to 4.24 mM NaN_3. Eq. (8) was fitted to each reaction mixture spectrum, employing the spectra of the pure compounds $MbFe^{3+}$ (S_S) and $MbFe^{3+}N_3^{1-}$ (S_P) as the independent fitting variables (spectra are shown in the graphs). The [NaN_3]-resolved product formation curve calculated from the "percent of conversion" $C_{\%}$ is shown in Fig. 14. The residuals of the fitting are shown below the spectra. Frequency: 9.23 GHz; modulation amplitude: 1.0 mT; microwave power: 2 mW; temperature: 18 K. Each spectrum is an average of two acquisitions.

using X-band EPR spectroscopy. The EPR spectra were corrected for the baseline by weighted polynomial fitting as described in Experimental procedures, and EfC-normalized as described above. To calculate the percent of conversion, the normalized mixed spectra (Fig. 13, 1–10) were deconvoluted in two components, S_S and S_P, using Eq. (8); the fitting residuals are shown in Fig. 13 (R1–R10). The calculated trace is shown in Fig. 14, together with the corresponding trace derived from the low-temperature optical absorbance measurements. The experimental data points closely overlap, and the fitted τ_a^{fit} values agree within 15% error.

Table 4
Comparison of the calculated values of the sample-ageing time (τ_α^{calc}) to the fitted values (τ_a^{fit}) calculated from Eqs. (3)–(6)

SF		MHQ	
$\tau_\alpha^{calc\dagger}$	τ_a^{fit}	$\tau_\alpha^{calc\ddagger}$	$\tau_a^{fit\P}$
2.7 s	2.2 ± 0.06 s	2.47 ± 0.026 ms	2.07 ± 0.17 ms
0.9 s	0.87 ± 0.03 s	1.07 ± 0.026 ms	0.43 ± 0.03 ms
0.3 s	0.29 ± 0.02 s	562 ± 26 µs	233 ± 12 µs
0.15 s	0.14 ± 0.01 s	227 ± 26 µs	167 ± 8 µs
70 ms	64 ± 5 ms	134 ± 26 µs	137 ± 18 µs
30 ms	30 ± 3 ms		
16 ms	20 ± 3 ms		
8 ms	9.9 ± 1.9 ms		

† From the time scale of the SX-18 software package.

‡ Calculated taking into account the values of the volumetric flow rate, volume of the mixing chamber, jet speed and the uncertainty of the spraying distance.

¶ Determined taking $T_a^{fit} = 8.2 \pm 0.2$ °C.

From Table 4 it follows that the sample-ageing time decreases with the decrease of the jet length and an increase of the jet speed. However, at fixed jet speed (~ 117 m s^{-1}) some deviation from the proportionality of the time-distance correlation can be clearly seen (Fig. 15). For example, at ~ 28 cm the fitted sample-ageing time τ_a^{fit} is ~ 16% shorter than the τ_a^{calc} value obtained from Eq. (1), at ~ 12 cm it is 60% shorter, at ~ 6 cm it is ~ 59% shorter, at 2.3 cm it is shorter by ~ 26%, while at 2 cm and 187 m s^{-1} the calculated value equals to the estimated value within the experimental error (Table 4). The reason stems from the fact that T_a^{fit}, the fitted average reaction

temperature, which we estimated as shown in Fig. 10, does not take into account the distance-dependent jet cooling. "Overcooling" of the sample jet at intermediate distances leads to "underreacting" of the sample, causing an apparent "decrease" of the sampleageing time. On the other hand, at long distances and medium jet speeds, (a) the air resistance at 150 mbar pressure causes a slow-down of the jet by 10–15%, and (b) expansion of the jet cone leads to a decrease of jet momentum per unit of surface of the cryomedium, slowing down the heat transfer during quenching. Both of these phenomena cause an apparent increase of the transit time and "overreacting" of the sample. "Overreacting" due to increase of the transit time partly counterbalances the "under-reacting" due to overcooling, and the fitted values τ_a^{fit} approach the calculated values τ_a^{calc}. The effects of overcooling, jet slow-down, and cone expansion become insignificant at short distances, when rapid jets are used (20–30 mm, 150–200 m s^{-1}). Under these conditions, τ_a^{fit} and τ_a^{calc} converge within experimental error.

To conclude, at shortest possible distance (~ 20 mm) and the highest jet speed values (~ 187 m s^{-1}), the sample-ageing time comes down to τ_a= 137 ± 18 μs (trace 12), which can be considered as the "dead" time of the MHQ prototype presented in this paper.

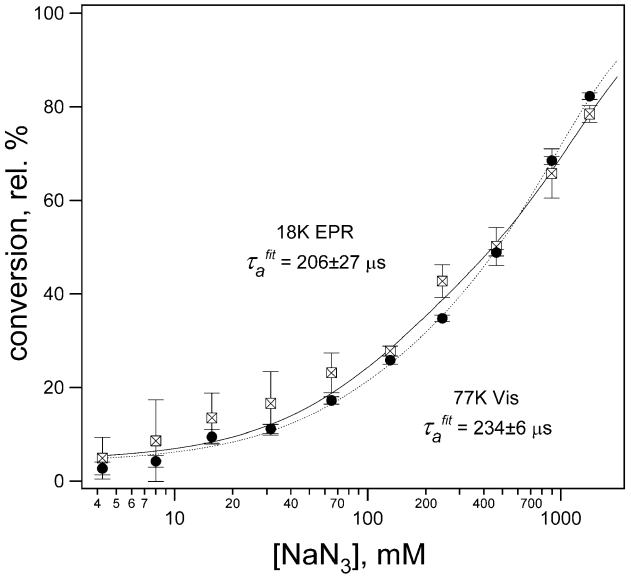

Fig. 14. [NaN_3]-resolved product formation curves for the metmyoglobin–azide binding reaction. MHQ samples were obtained at different concentrations of sodium azide and a distance to the cryomedium surface of 6.2 cm. The sample volumetric flow rate was 2.0 ml min^{-1} (~ 117 m s^{-1}). Final concentrations are [$MbFe^{3+}$]—0.73 mM; [NaN_3]—4.24 mM, 8.01, 15.62, 31.45, 64.99, 131.1, 243.97, 464.24, 898.58 mM, and 1.415 M, pH = 5. Closed circles—the values obtained from the analysis of the 77 K optical absorbance spectra. Crossed squares—18 K X-band EPR spectra. Solid and dotted traces were obtained by fitting Eq. (9) to the experimental data, using sample-ageing time as the fitting parameter (fitted values are shown in the graph).

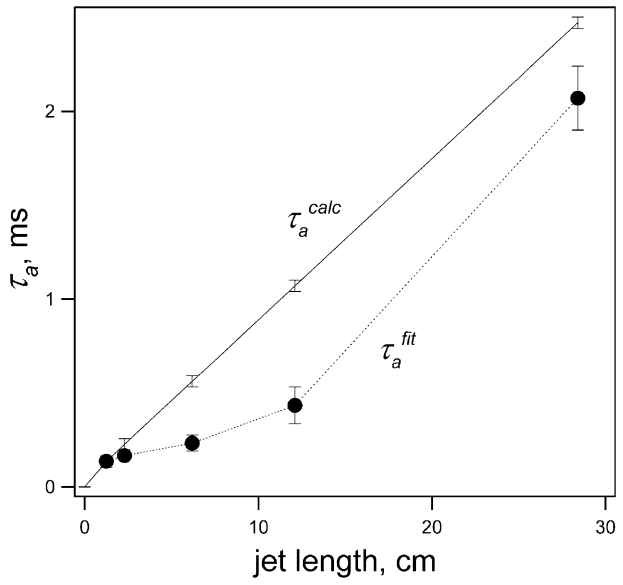

Fig. 15. Dependence of the sample-ageing time on the jet length at 117 m s^{-1} jet speed. Jet length was measured as the distance between the micromixer and the surface of the cryomedium. τ_a^{calc} values were obtained using the linear flow velocity values determined from the volumetric flow rate and the orifice diameter, plus the 10% increase of the linear flow velocity as measured by LDA. τ_a^{fit} values were obtained by fitting Eq. (9) to the traces 9–13 shown in Fig. 12. To show in the graph the τ_a^{fit} value for the trace 13, the distance was decreased to 1.25 cm to account for higher jet speed of 187 m s^{-1}.

2.9. Reaction intermediate in the metmyoglobin–azide binding reaction

As was mentioned above, reaction intermediates can be detected in the freeze-quench samples during the two-component deconvolution of their electronic absorbance into the spectra of the "starting material" and of the "end product". If a third absorbing component is present in the reaction mixture it will show itself during fitting as non-zero residuals, with the maximum perturbation corresponding to the wavelengths of maximal/minimal absorbance of the intermediate. In the case of the metmyoglobin–azide reaction couple, we were able to detect the signature of a transient intermediate at the shortest freeze-quench times (~ 137 μs, d ~ 20 mm and the jet speed ~ 187 m s^{-1}). It appeared as a pronounced deviation from linearity in the whole absorbance envelope (Fig. 16A). In Fig. 16B we show the comparison between the spectra of the "130 μs" sample and the similar spectra obtained after ~ 430 μs (also see Fig. 12, encircled data points). In the latter case, the myoglobin reacted for longer time but with less azide present, that is why the degree of conversion is almost the same. The features can be seen even better after calculating the difference spectrum ["130 μs" min "430 μs"] (Fig. 16C, lower trace), which appears to be very similar to the fitting residuals of the "130 μs" spectrum (Fig. 16C, upper trace). The transient intermediate is characterized by an overall decrease of the absorbance at 500–700 nm, 3-nm blue shift of the charge transfer band at 503 nm, a 2.5-nm red

shift of the charge transfer band at 544 nm, and a shift of the α- and β-bands halfway between their position in the spectrum of the free metmyoglobin and the spectrum of the metmyoglobin–azide complex (Fig. 16C, Table 5). The perturbation intensity reaches approximately 20% of the overall spectral intensity at an azide concentration of 759.6 mM (Fig. 16A). The observed azide binding rate at this

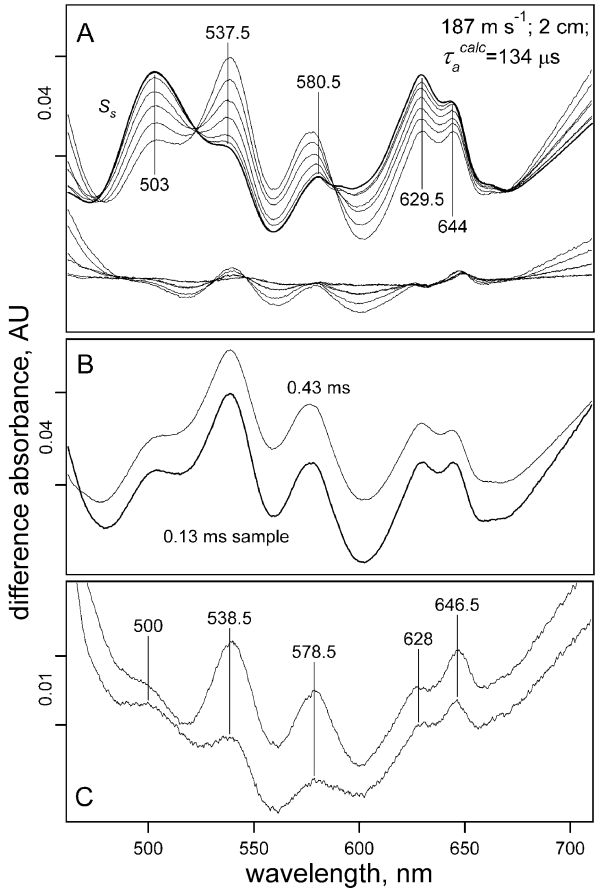

Fig. 16. Formation of the transient reaction intermediate in the course of the metmyoglobin–azide binding reaction and its spectral characteristics. A. Baseline-corrected and EfC-normalized 77 K optical absorbance spectra of the freeze-quenched metmyoglobin–azide reaction samples, obtained at a spraying distance of 2 cm, and a sample volumetric flow rate of 3 ml min^{-1} (~ 175 m s^{-1}). Final concentrations are [$MbFe^{3+}$] = 0.73 mM; [NaN_3]—30.21, 57.03, 109.9, 212.3, 395.3, and 759.6 mM, pH = 5. Eq. (8) was fitted to each reaction mixture spectrum, employing the spectra of pure compounds S_S and S_P as the independent fitting variables. The residuals of the fitting are shown below the spectra. (B) Normalized spectra of the reaction samples prepared at a similar percent of conversion. "0.43-ms" spectrum was obtained from the reaction sample, which was prepared by mixing the components to the final concentration of [$MbFe^{3+}$] = 0.73 mM, and [NaN_3]—243.97 mM, pH = 5 and spraying from the distance of 6.1 cm with the volumetric flow rate of 2 ml min^{-1} (~ 117 m s^{-1}). "0.13-ms" spectrum was obtained from the sample prepared at the conditions as follows: [$MbFe^{3+}$] = 0.73 mM, [NaN_3]—759.64 mM, pH = 5, distance d = 2.0 cm, the volumetric flow rate of 3.2 ml min^{-1} (~ 186 m s^{-1}). The values for the percent of conversion for these samples are encircled in the Fig. 12. (C) Upper trace—residuals of the fitting of the Eq. (8) to the 0.13-ms sample shown in (B). Lower trace—the difference spectrum [0.13 ms minus 0.43 ms].

Table 5
Optical properties of the metmyoglobin, and metmyoglobin–azide complexes in the α- and β-band spectral region (Figs. 11A–D and 15C)

	λ, nm				
$MbFe^{3+}{\cdot}H_2O$	503	537	580.5	629.5	643
$MbFe^{3+}{\cdot}N_3^{1-}$ transient	500	538.5	578.5	628	646.5
$MbFe^{3+}{\cdot}N_3^{1-}$		539.5	571		

$[N_3^{1-}]$ can be estimated as $k_{obs} \sim 3.58 \times 10^3$ s^{-1} at 8.2 °C, suggesting that the intermediate decays with $k_{app} \sim 1.2 \times 10^4$ s^{-1}, i.e. has a half-life time of ~ 60 μs.

2.10. Pre-steady state kinetics of electron transfer in *Escherichia coli bo₃ oxidase*

Cytochrome *c* oxidase and cytochrome *bo₃* oxidase catalyse the electron transfer from *c*-type cytochromes and quinols, respectively, to molecular oxygen. They belong to the superfamily of haem-copper oxygen reductases [185] and are evolutionary related to NO reductases [186,187]. In the physiological sense, haem-copper oxidases serve as terminal electron acceptors in the bioenergetic metabolism of all aerobic organisms. These membrane-bound metalloenzymes couple electron transfer to proton pumping, thereby converting the redox free energy ΔG_{redox} of the overall reaction in a proton motive force ($\Delta\mu H^+$), which can be used to drive ATP synthesis or to transport ions, metabolites and macromolecules, see, e.g. Ref. [188].

The overall reaction of cytochrome *c* oxidase and cytochrome *bo₃* oxidase is given by the following reaction (Eq. (I))188).

$$4\text{cyt.}c^{2+}/2QH_2 + 8H_C^+ + O_2 \rightarrow 4\text{cyt.}c^{3+}/(2Q + 4H_P^+) + 4H_P^+ + 2H_2O \quad \text{(I)}$$

The highly complex molecular mechanism of action of heme-copper oxidases—involving at least 13 elementary steps—has been the focus of attention of many researchers for more than seven decades. We do not intend here to survey the literature but refer the reader to recent reviews on oxidases and the references therein [189–195].

The crystal structures of several oxidases are now available [196–202]. The structural information supports the picture obtained from a wealth of bioenergetic experimentation that protons (8 H_C^+) and electrons (4 cyt. c^{2+}/2 QH_2) enter the oxidase from different sides of the membrane (see Eq. (I)), protons coming from the cytoplasm (mitochondrial matrix) and electrons from the periplasm (inter membrane space). The quinol substrate protons (H_P^+) are not translocated, so, although the measured proton/electron ratio (H^+/e) equals 2 and 1 for quinol and cytochrome *c* oxidases, respectively, the true number of translocated charges is the same (q/e = 2). For both types of enzymes, four cytoplasmic protons (4 H_c^+) combine with four electrons at the binuclear active site yielding water, the so-called chemical protons. The other four protons are translocated across the mem-

brane, the so-called pumped protons. The two types of protons may follow different routes through the enzyme; see, e.g. Ref. [203]. The measured H^+/e may be dependent on the buffer, but some oxidases, including those from archaea, may pump less than four protons [204–207]. For the remainder of the overview, we will focus only on the kinetics of electron transfer, and will not discuss protonation reactions.

All oxidases have a similar active site, a binuclear center consisting of an iron (heme a_3 (o_3, b_3)) and a copper (Cu_B) ligated by three histidine residues. One of the histidine residues is covalently linked to a nearby tyrosine (YOH, see Fig. 17) and located in the vicinity of heme a_3 or o_3. The distance between the heme iron and copper is around 4.5–5 Å.

The overall cycle of oxygen reduction catalyzed by oxidases is too rapid to be monitored by conventional stopped-flow or rapid freeze-quench techniques, about 1 ms at physiological temperatures [208]. To circumvent the problem of rapid mixing of the reduced enzyme with dioxygen, two highly elegant techniques were developed over the years, the flow-flash method [209,210] and the triple trapping method [211]. In both techniques partially or fully reduced cytochrome oxidase is prepared in the presence of CO. The CO-inhibited enzyme is mixed with an oxygenated solution creating a metastable state, which relaxes via "displacement" of CO and oxidation of the enzyme on seconds-to-minutes time scale. However, before any appreciable amount of enzyme is oxidized, turnover of the oxidase is triggered by CO flash photolysis, within nanoseconds yielding the reduced enzyme ready to react with dioxygen, thus obviating the need for rapid mixing. In the flow-flash method, CO-inhibited oxidase and oxygenated buffer are mixed in a pneumatically driven mixing device and the reduction of dioxygen is monitored after a flash of light using UV–Vis spectrometry [92–95,212–214]. For resonance Raman spectroscopy, the sample flows in a small flow cell, and, after photolysis at a particular spot, the time course of the reaction is followed by exciting the reacting groups with a (second) laser at various positions of the cell [215–217]. In the triple trapping method, which is performed at low temperatures

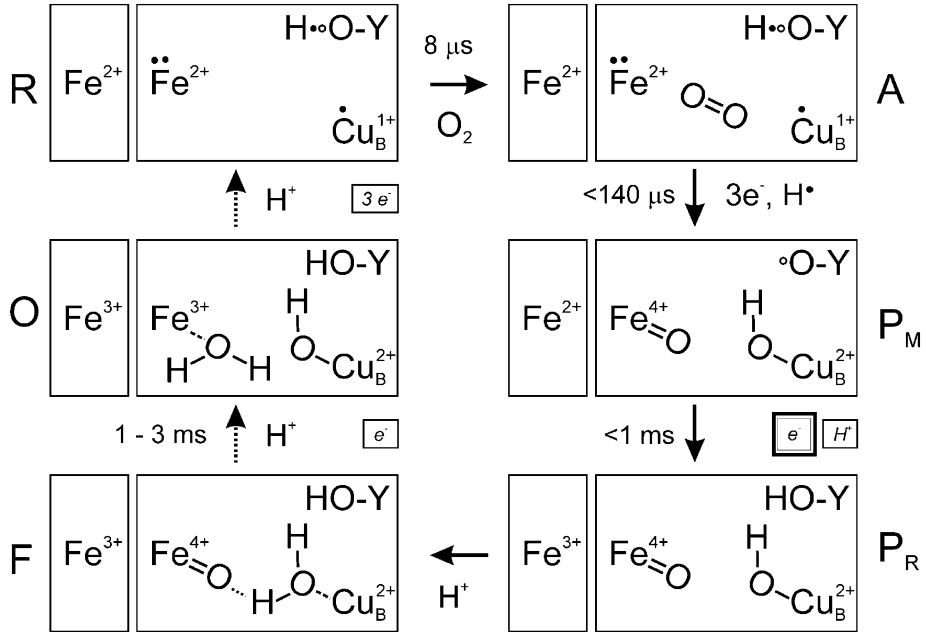

Fig. 17. Structures of intermediates formed during the reaction of terminal oxidases with dioxygen. Modified from Ref. [91], and adapted for the three-electron reduced bo_3 ubiquinol oxidase from *E. coli*. The reduced binuclear center is represented by Fe^{2+} and Cu^{1+}, denoting heme o_3 (or a_3) and Cu_B, respectively. Iron of heme *b* (or *a*) is shown to the left of the binuclear center. The covalently cross-linked tyrosine–histidine pair is shown as YOH, its neutral radical form as YO°. The electrons in the binuclear center that are donated to oxygen are denoted with (●). In case when **R** represents the mixed-valence (two-electron reduced) state, the reaction proceeds from **R** via **A** and stops at $\mathbf{P_M}$. If **R** represents the fully reduced (four-electron reduced) state, the reaction proceeds via **A**, $\mathbf{P_M}$, $\mathbf{P_R}$ to **F**, which is slowly converted (*via* several intermediates) to the oxidized enzyme, **O**. Heme *b* (bo_3 oxidase) or *a* (aa_3 oxidase) donates an electron to the tyrosine radical in the binuclear center in the conversion from $\mathbf{P_M}$ to $\mathbf{P_R}$. When **R** represents the three-electron reduced enzyme, as in quinone-free fully reduced cytochrome bo_3, a radical intermediate is formed within 130 μs with optical properties similar to that of (a mixture of) **P** and **F** species, (Fig. 18). It is assigned to the $\mathbf{P_M}$ species, because it contains a radical, and, presumably, is formed directly from **A**. $\mathbf{P_M}$ is converted to $\mathbf{P_R}$ and/or **F** by electron transfer from heme *b* with a half time of 400–500 μs (Figs. 17 and 18). NB: Specific electron transfer to the oxygen substrate and corresponding protonation events are denoted with large capitals. External input of electrons to the enzyme and corresponding protonation events are denoted in small italics. Internal electron transfer from heme *b* (or *a*) to the tyrosine radical in the binuclear center is denoted with the dark framed box. Steps that include multiple intermediates are denoted with dotted arrows. Specific protonation and proton translocation events that are related to the proton-pumping oxidase activity have been omitted from the figure. Reaction rates $\mathbf{R} \rightarrow \mathbf{A}$ and $\mathbf{F} \rightarrow \mathbf{O}$ are taken from Ref. [91] and relate to cytochrome *c* oxidase; the values <140 μs for $\mathbf{A} \rightarrow \mathbf{P_M}$, and <1.08 ms for $\mathbf{P_M} \rightarrow \{\mathbf{P_R}, \mathbf{F}\}$ were obtained in this study on the bo_3 oxidase (Figs. 17 and 18). See text for further details.

with a transparent sample (e.g. an ethylene glycol glass), the kinetics can be followed by UV–Vis spectrometry following flash photolysis, and the sample can be quenched at any time, e.g. frozen in liquid nitrogen and subsequently monitored by EPR [211,218–221].

For experimentation, the cytochrome *c* oxidase can be prepared in either of two states: the fully reduced state containing four electrons, or the half reduced (mixed-valence) state with two electrons. In addition to that, cytochrome bo_3 ubiquinol oxidase can be prepared as a three-electron enzyme, when it is purified without the ubiquinone cofactor [222,223].

Fig. 17 summarizes the current view of the initial steps in oxygen reduction [91,192,224], and in addition includes our present findings and suggestions. The oxidase (either mixed-valence, three- or four-electron reduced) initially resides in the **R** state, in which the binuclear center itself already has four electrons necessary for the reduction of oxygen, two electrons at heme o_3 (a_3), one electron at Cu_B^I, and a hydrogen atom at the tyrosine–histidine pair. Upon binding of dioxygen in the binuclear center, **R** is rapidly converted to the oxygenated intermediate **A**. The actual reduction of dioxygen occurs in the next reaction step, when (a) the donation of a hydrogen atom from the nearby tyrosine–histidine pair splits the O=O bond, forming the neutral radical YO*, (b) donation of an electron from Cu_B^I results in the formation of the Cu hydroxide, Cu_B^{II}-OH, and (c) donation of two electrons from heme o_3 (a_3) results in the formation of the oxoferryl complex, Fe^{IV}=O. After this four-electron oxidation step, the enzyme ends in the high-energy intermediate $\mathbf{P_M}$ state, in which all of ΔG_{redox} is trapped. The name $\mathbf{P_M}$ originates from the fact that it was once thought to be a **P**eroxy intermediate, and it was first observed in the **M**ixed valence (two-electron reduced) enzyme [225]. Currently, there is general agreement regarding the structure of $\mathbf{P_M}$. Together with the intermediate **A**, it has been first identified by the triple trapping method [211]. Its structure (and that of **A**) has been confirmed by resonance Raman spectroscopy [215,226,227], showing that $\mathbf{P_M}$ represents an oxoferryl state of heme a_3, Fe^{IV}=O. Subsequently, a tyrosine radical in the $\mathbf{P_M}$ state has been identified, using radioactive iodide labeling of cytochrome *c* oxidase followed by peptide mapping [228]. $\mathbf{P_M}$ is a transient metastable state; the enzyme relaxes to the resting oxidized form **O** via a series of inter/intra/molecular heme–protein and heme–heme electron transfers and protonation events. For example, donation of an electron from heme *a* (or *b*) to the tyrosine radical and subsequent protonation leads to the formation of the $\mathbf{P_R}$ state, which, after protonation of the oxygen in the Cu_B^{II}-OH, yields the reaction intermediate **F**. Intuitively, the relaxation kinetics are supposed to be the fastest in the case of the four-electron reduced enzyme, while in the case of the mixed-valence enzyme, the $\mathbf{P_M}$ state, in principle, can be captured under

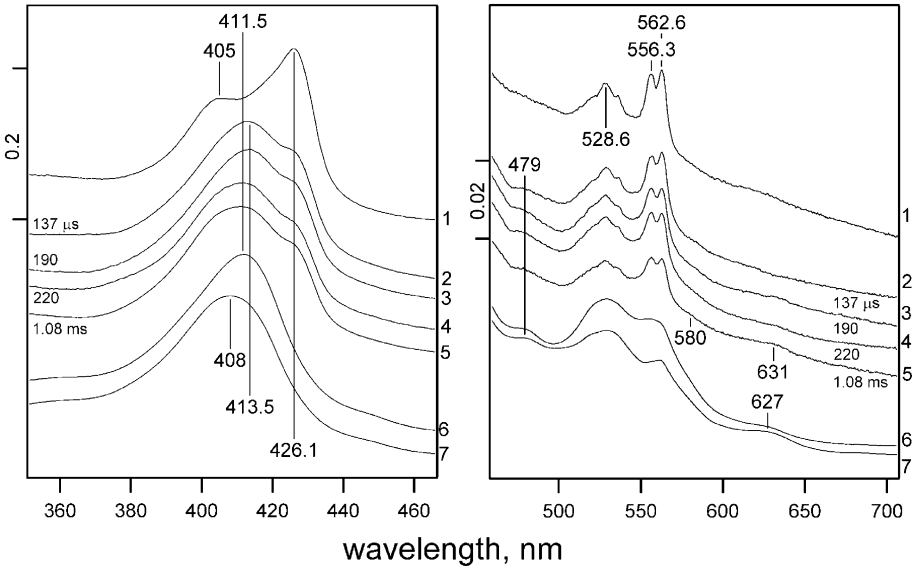

Fig. 18. 77 K optical absorbance spectra of the MHQ samples of cytochrome bo_3 ubiquinol oxidase obtained in the course of the reaction with dioxygen. *Spectrum 1—"reduced bo_3 oxidase"*—obtained by mixing ~ 150 μM enzyme solution with an anoxic solution of 10 mM ascorbate, 5 μM PES in 60 mM K-phosphate buffer, 0.5 M KCl, pH = 7.5 at a flow rate of 3.2 ml min^{-1} (187 m s^{-1}), d = 20 mm; *spectrum 2—"137 μs sample"*—reduced bo_3 oxidase mixed with 100% O_2 saturated buffer at a flow rate of 3.2 ml min^{-1} (187 m s^{-1}), d = 20 mm; *spectrum 3—"190 μs sample"*—ibid. at a flow rate of 2.6 ml min^{-1} (152 m s^{-1}), d = 38 mm; *spectrum 4—"220 μs sample"*—ibid., d = 53.2 mm; *spectrum 5—"1.08 ms sample"*—ibid., d = 253 mm. Concentrations after mixing: ~ 0.5 mM O_2 and ~ 75 μM bo_3 oxidase. The EfC of the enzyme in the cuvette is ~ 3 ± 0.3 μM. Each trace represents the average of 20 acquisitions. Reduced bo_3 ubiquinol oxidase was prepared as described in Experimental procedures. Spectrum 6—"mixture of **P** and **F**-like species"—oxidized bo_3 oxidase, diluted to 10 μM in 50 mM K-phosphate, 0.5 M KCl, pH = 7.5 in the presence of 10 mM H_2O_2 and frozen by injecting into the pre-cooled cuvette at 77 K within ~ 30 s after mixing with peroxide. *Spectrum 7—"oxidized bo_3 oxidase"*—ibid., in the absence of H_2O_2. Due to the large difference of absorbance values in the Soret region and the α-β-band region, the same spectra are shown in two, separately scaled graphs. (*) The sample-ageing times were estimated (at 8.2 °C) using the calibration values shown in Table 4.

stoichiometric reaction conditions. $\mathbf{P_R}$ and **F** are oxoferryl intermediates as well, having an extra electron in the binuclear center (Fig. 17). EPR and ENDOR spectroscopy of cytochrome *c* oxidase in the mixed **P** and **F**-like state, performed after equilibration of the enzyme with H_2O_2, showed low levels of radical signals ascribed to a mixture of tryptophan (or cysteine) and porphyrin cation radicals [229–231], or in case of *Paracoccus denitrificans* oxidase, to a tyrosine radical, which most likely does not derive from the tyrosine–histidine pair [232].

Until the studies reported here, the radicals have been prepared on a seconds-to-minutes time scale, under (pseudo)-equilibrium conditions. In an attempt to follow the formation of kinetically competent radical intermediates, we have applied the MHQ technique for studies on the oxidation of quinone-free three-electron reduced cytochrome bo_3 oxidase from E. coli. The preliminary results are shown in Figs. 17 and 18. Our first data point is obtained after ~ 137 μs (Fig. 18-2), so the formation of **A** should be complete, because it is formed with a rate constant of 3.4×10^4 s^{-1} or $\tau_{1/2} = 20.4$ μs [223,233,234]. After 137 μs, about 50% of the absorbance at 426.5 nm disappears concomitant with the formation of a peak at 413.5 nm. This is consistent with oxidation of heme o_3^{2+} and formation of the oxoferryl species [223,233]. The intensity at 426.5 nm decreases only slightly between 137 μs and 1.08 ms, while the peak absorbance maximum at 413.5 nm shifts to 411.6 nm (Fig. 18 (2–5)). A similar spectrum is obtained after incubation of bo_3 oxidase with H_2O_2, which is a mixture of oxoferryl **P** and **F** states (Fig. 18-6) [229,235–237]. In the α-band region, a small decrease in absorbance at 556 and 562.6 nm occurs in the first 137 μs, consistent with the oxidation of heme o_3^{2+}; these small changes are consistent with a weak spectral contribution of heme o_3 in this region. The absorbance intensity between 545 and 575 nm is dominated by the split α-band of heme b^{2+}, and it can be seen that between 137 μs and 1.08 ms, some 20–40% of heme b^{2+} is oxidized. In addition, small absorbance changes are observed around 580 and 631 nm.

For the first time in studies on oxidase catalysis, the direct reduction of dioxygen observed by EPR spectroscopy showed the formation of a transient radical after 137 μs, which decays within 1.08 ms (Fig. 19 (3–6)). The radical is centered at g = 2.004–2.005, and has an apparent peak-to-peak width of 1.4 mT; owing to its low concentration, the signal has to be recorded at saturating microwave power). At present, the signal to noise is too poor to assign the radical to a specific amino acid, viz. YO*. The line shape seems, however, different from the tyrosine radical observed in *Pa. denitrificans* oxidase or in 2-imidazol-1-yl-4-methylphenol, an analog of the tyrosine–histidine pair [232,238]. The shape is more similar to that obtained in [229,230,239], but it is not identical. We cannot conclude at present whether the signal represents a pure species or a mixture. The signal is also different from that of the small amount of radical formed in the presence of H_2O_2, which has a peak-to-peak width of 1.1 mT (Fig. 19-7). Given (i) the poor signal-to-noise ratio, (ii) the saturating power used potentially causing changes in the line shape, (iii) the uncertainty about the spectral envelope, and (iv) the variations in sample concentration inherent in the MHQ technique, the concentration of the radical is estimated at 0.2–0.4 spins per cytochrome bo_3. Because this is similar to the extent of oxidation of heme *b*, we propose that the electron from heme *b* reduces the radical, consistent with the reduction of $\mathbf{P_M}$ to the $\mathbf{P_R}$ state, or, as earlier suggested to **F** [223,233].

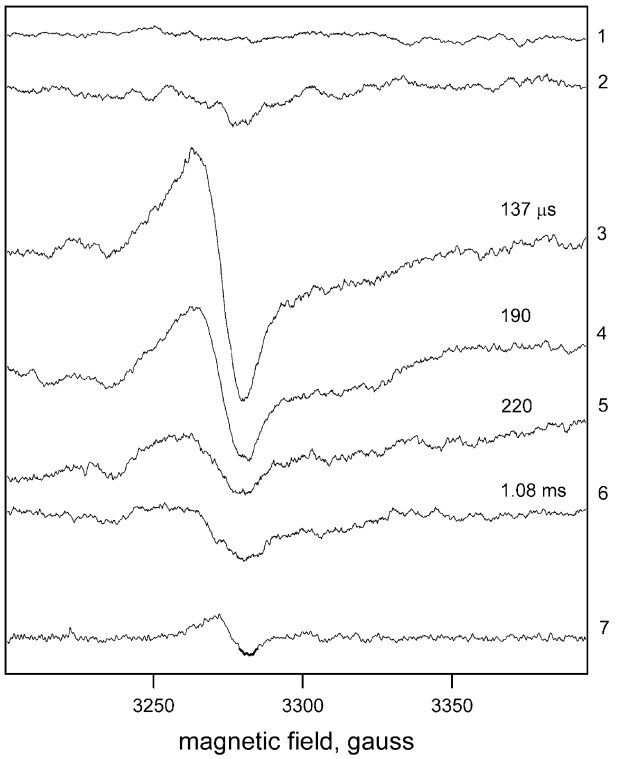

Fig. 19. X-band EPR spectra of the MHQ samples of cytochrome bo_3 ubiquinol oxidase obtained in the course of the reaction with dioxygen. *Spectrum 1—"Blank"*—MHQ preparation of anoxic buffer containing 60 mM K-phosphate, 0.5 M KCl, 10 mM ascorbate, and 5 mM PES at pH = 7.5, freeze-quenched at a flow rate of 3.2 ml min^{-1} (187 m s^{-1}), $d = 20$ mm; *spectrum 2—"reduced bo3 oxidase"*— ~ 150 μM enzyme solution is mixed with an anoxic solution of 10 mM ascorbate, 5 μM PES in 60 mM K-phosphate buffer, 0.5 M KCl, pH = 7.5 at a flow rate of 3.2 ml min^{-1} (187 m s^{-1}), $d = 20$ mm; *spectrum 3—"137 μs sample"*—ibid., but mixed with 100% O_2 saturated buffer at a flow rate of 3.2 ml min^{-1} (187 m s^{-1}), $d = 20$ mm; *spectrum 4—"190 μs sample"*—ibid. at a flow rate of 2.6 ml min^{-1} (152 m s^{-1}), $d = 38$ mm; *spectrum 5—"220 μs sample"*—ibid., $d = 53.2$ mm; *spectrum 6—"1.08 ms sample"*—ibid., $d = 253$ mm. Concentrations after mixing: ~ 0.5 mM O_2 and ~ 75 μM bo_3 oxidase. The EfC of the enzyme in the EPR tube is ~ 11 ± 1 μM. Spectrum 7—"mixture of **P** and **F**-like species"—oxidized bo_3 oxidase, diluted to 11 μM in 50 mM K-phosphate, 0.5 M KCl, pH = 7.5 in the presence of 10 mM H_2O_2, transferred into the EPR tube and frozen by immersion in LN_2 within ~ 60 s after mixing with peroxide. EPR conditions: Frequency: 9.25 GHz; modulation amplitude: 0.63 mT; microwave power: 2 mW; temperature: 35 K. NB: To improve the signal to noise ratio each trace is an average of five EPR spectra recorded under slightly power saturating conditions.

In two-electron reduced cytochrome *c* oxidase, a $\mathbf{P_M}$ state containing a tyrosine radical has been previously identified [228]. Our preliminary data show direct evidence for the presence of a kinetically competent radical in the case of the three-electron reduced cytochrome bo_3 oxidase as well. The radical is formed transiently upon oxidation of heme o_3 and it decays following the oxidation of heme *b*. The optical absorbance spectra show that the oxoferryl species is formed concomitantly with the radical; therefore, the radical can be assigned to the $\mathbf{P_M}$ reaction intermediate, implying that the oxidation step $\mathbf{A} \rightarrow \mathbf{P_M}$ occurs in the case of three-electron reduced enzyme, similar to the mixed-valence oxidase.

In the case of four-electron reduced cytochrome *c* oxidase, it was suggested that the reduction of the dioxygen in the **A** state leads to the formation of the $\mathbf{P_R}$ intermediate [91,192,224,240] bypassing the radical-containing $\mathbf{P_M}$ state. However, given the important mechanistic role played by the tyrosine residue as the donor of the H-atom for the O=O bond splitting [215,228], it seems unlikely that reduction of dioxygen would proceed differently in the four-electron reduced enzyme compared to either two- or three-electron reduced enzyme. We therefore propose the reaction sequence $\mathbf{R} \rightarrow \mathbf{A} \rightarrow \mathbf{P_M} \rightarrow \mathbf{P_R} \rightarrow \mathbf{F}$ to be the compulsory catalytic pathway for all cytochrome oxidases, irrespective of the oxidation state of the **R** species. In principle, this proposal is in agreement with the mechanism of the O=O bond splitting proposed in Ref. [241]. The fact that $\mathbf{P_M}$ has not been observed so far in four electron-reduced cytochrome *c* oxidase might be due to (a) the identity of the spectra of the $\mathbf{P_M}$ and $\mathbf{P_R}$ states as seen by optical absorbance spectroscopy [91,242], and (b) general lack of efficient experimental techniques for detection of short-living radical species in biological systems.

2.11. Concluding remarks and future prospects

In this review, the development and applications of a novel microsecond freeze-hyperquenching mixing and sampling methodology—MHQ, have been described. The current setup makes it possible to obtain samples with ageing times in the 100–150 μs time domain and analyze them by low-temperature UV–Vis and EPR spectroscopy. Nontransparent freeze-quenched reaction samples can be analyzed by low-temperature UV–Vis spectroscopy in the spectral region above 300 nm, with a resolution of signal intensity of 5×10^{-3} AU and a spectral precision of 0.5 nm. The high sensitivity of low-temperature UV–Vis spectroscopy and the option to acquire multiple scans not only allow detection of the highly absorbing heme-iron active sites, but also of sites with lower extinction coefficients, such as iron–sulfur clusters, copper sites, flavins, non-heme iron centers, diiron centers, etc.

The improvement in time resolution of mixing, sample transport, and freeze-quenching processes has been achieved using a specifically designed four-jet tangential micro-mixer operating at high pressures c.q. high linear flow rates. Due to the small diameter of the sample jet and high jet velocity, efficient quenching of the reaction in the MHQ apparatus occurs in microseconds. The additional specific benefit of hyperquenching includes maximal preservation of the structure of the reaction intermediates, of the protein, protein–protein, or protein–ligand complexes during freezing under vitrifying conditions similar as in cryo-electron microscopy.

The use of a tangential micro-mixer allows efficient mixing of concentrated protein solutions; sample delivery by HPLC pumps gives the possibility to prepare large amounts of sample (up to 1–2 ml), enabling MHQ to be used in conjunction with sample-consuming techniques as FTIR or Mössbauer spectroscopy.

Even though the characteristic "dead" time of the MHQ device is more than 35-fold shorter in comparison with the conventional rapid freeze-quench instruments, several improvements in time resolution could still be made. About three times higher linear flow rates (500–600 m s^{-1}, 4–6 kbar) can be used because most enzymes start to unfold/irreversibly denature only at pressures above 5 kbar [243–247]. Use of jets with smaller diameters (5–10 μm) can result in faster cooling compared with ~ 30 μs for a 20-μm jet. Finally, a major improvement of the time resolution can be obtained by freeze-quenching the reaction mixture on a cold plate instead of a liquid cryomedium, because the sample transport distance can be decreased ~ 10-fold to 2 mm. A cold plate MHQ setup has been assembled, and is currently being tested in Delft. We expect that MHQ or similar technology will allow preparing samples with ageing times ultimately within 5–10 μs.

One of the great advantages of the MHQ technique is the unique opportunity to analyze the same sample by a number of spectroscopic techniques, thereby greatly increasing its analytical potential. For the near future we foresee applications in high frequency EPR, FTIR, resonance Raman, EXAFS, MAS-NMR, and Mössbauer spectroscopy. Currently, the dilution of the sample in the cryomedium and the electrostatic nature of the fine protein powder have been severely limiting analysis of the freeze-quenched samples by these spectroscopic techniques, with the exception of resonance Raman spectroscopy.

The power of MHQ is illustrated well by the results obtained with the two examples detailed in this work, binding of azide to metmyoglobin from horse heart, and reduction of dioxygen by cytochrome bo_3 ubiquinol oxidase from *E. coli*. In both cases, (novel) rapidly formed transient intermediates have been detected, and their kinetic and spectral properties characterized. In the near future, we expect application of MHQ for studies on molecular mechanisms of catalysis not only of metalloproteins but also of any enzyme that is changing its spectroscopic signature during turnover. MHQ may well prove to be one of the key approaches in the scientific developments towards understanding the laws of structure–function relationship in the uniquely evolved biological catalysts, the enzymes.

3. Experimental procedures

3.1. Chemicals

Metmyoglobin from horse heart and 2-hydroxycinnamic acid were purchased from Sigma Aldrich NV, isopentane was supplied by Fluka Biochemicals, Triton X-100 and β-octyl glucoside was from Sigma, β-dodecyl maltoside originated from Anatrace. Argon (6.0 grade) was used for the anaerobic maintenance and operation of the freeze-quench instrument.

3.2. Purification of cythochrome bo_3 oxidase

Ubiquinone-free cytochrome bo_3 oxidase from *E. coli* was prepared essentially according to Rumbley et al. [222]. For exchange of Triton X-100 and β-octyl glucoside, the enzyme was additionally passed through the POROS HQ column (70 ml) pre-equilibrated with 25 mM K–phosphate buffer in 0.05% β-dodecyl maltoside (LM), pH = 8.3 (Buffer A). The column was washed with at least 30 column volumes of buffer A until the absorbance at 260 nm of Triton-X100 subsided; the enzyme fraction was subsequently eluted in 10 column volumes of a linear gradient 0–1 M of NaCl in buffer A. The enzyme fraction was concentrated to a 25 mg ml^{-1} (~ 170 μM) solution, desalted to 10 mM K-phosphate, pH = 7.5, 0.05% LM using 100-kDa cutoff CentriPrep concentrators (Amicon), and stored in aliquots of 300 μl at − 80 °C. The enzyme preparation was homogeneous for >96%; the enzyme contained heme *b* and heme *o* in a 1:1 ratio as previously described [248]. Approximately 200 mg of cytochrome bo_3 oxidase was purified from 2.3 kg wet weight of GO105 *E. coli* cells.

3.3. MHQ instrumentation

The freeze-quench setup (Fig. 2, 1–16) was assembled from parts obtained from different suppliers.

3.3.1. Sample loading and delivery

HPLC pumps (Fig. 2, 13-1, 13-2) were supplied by Waters Chromatography, Rheodyne-type sample injection valves (Fig. 2-12), PEEK sample delivery tubing (blue stripe), T-type connectors, 5-μm and 0.2-μm in-line solvent filters (Fig. 2-11), Hamilton sample loading syringes, and PEEK ferrule connectors originated from Supelco.

3.3.2. Vacuum maintenance

Low-pressure chamber (Fig. 2-1), RV5 oil vacuum pump (Fig. 2), Piranhi vacuum gauges, air admission valves, two-way valves, NW-type stainless steel vacuum lines, and AGC active vacuum gauge controller were purchased from Edwards. The base-plate for the low-pressure chamber (Fig. 2-9), and LN_2 trap (Fig. 2-10) were homemade.

3.3.3. Mixer, and mixer positioning

A stainless steel rod holder (Fig. 2-2) equipped with a 90° bracket swinging-arm (Fig. 2-3) was obtained from Oriel Instruments. The tangential micro-mixer (Fig. 2-3) was constructed in house (see Figs. 3 and 4). Platinum inlays were purchased from Provak GmbH.

3.3.4. Cryomedium storage

Stainless steel LN_2-grade dewars of 3, 2, and 1 l were purchased from Cambridge Instruments. Isopentane samples were prepared, cooled, and stored in the gastight 75-ml ultracentrifuge tubes from Beckman.

3.4. Operation of the MHQ setup

3.4.1. Preparation, and handling of the cryomedium

A cold isopentane bath for short-term storage of the samples and cryomedium was made in a 3-l dewar. Isopentane (~ 2 l) was cooled to 125 K by adding LN_2. For sample preparation, the Beckman ultracentrifuge tube was filled to the top with fresh isopentane at room temperature, tightly closed, and dipped into the isopentane bath for equilibration to 125 K (~ 15 min). Just before the evacuation, the tube was withdrawn from the bath, opened, and cold isopentane was rapidly poured into the sample collection vessel (Fig. 2-7) pre-cooled to 77 K. After cryofixation, the isopentane-sample suspension was transferred back in the tube pre-cooled to 77 K, closed and inserted in the 125 K bath for storage until further use.

3.4.2. Sample preparation

Reaction components were diluted to the concentrations and pH indicated in the figure legends. Different concentrations of sodium azide were prepared by serial ~ 2-fold dilutions of the pH-equilibrated ~ 3 M stock solution into the working buffer of the appropriate pH in the 50-ml polypropylene Falcon tubes. To calculate the dilution coefficients with high accuracy, solutions were weighed on analytical balances with 0.2 mg precision.

Three hundred microliters of the "enzyme" component and 1.5 ml of the "substrate" component were used for the preparation of each sample (total quenched sample volume—0.6 ml). The "substrate" and the "enzyme" solutions were filtered through a 0.22 μm filter (Corning). Prior to loading of the components, the "enzyme" solution was additionally cleared by sedimentation in an Eppendorf centrifuge at 14,000 rpm for 3 min. The reaction components were loaded via the Rheodyne-type sample injection valves, equipped with the sample-loading loops of the required volume (PEEK tubing, blue stripe). In the case of cytochrome bo_3 oxidase, the ionic strength of the enzyme solution was increased by addition of 1/10 volume of 0.5 M K–phosphate, 5 M KCl, pH = 7.5. The enzyme solution (~ 150 μM) was transferred in the gastight vessel; anoxic conditions were achieved after several cycles of degassing and purging with Ar gas. The enzyme

was reduced by addition of ascorbate and PES to a final concentration of 10 mM and 5 μM, respectively. The extent of reduction was monitored in situ by UV–Vis spectrometry at RT through the vessel walls. For the freeze-quenching experiments, 300 μl of reduced bo_3 oxidase were withdrawn in a O_2-free gastight Hamilton syringe and loaded in a Rheodyne-type injection valve, which was pre-purged with anaerobic solvent and, prior to loading, flushed with an anoxic 10 mM ascorbate, 5 μM PES solution in 20 mM K–phosphate buffer, pH = 7.5. To trigger the reaction, the oxidase solution was mixed in 1:1 ratio against 60 mM K-phosphate buffer, 0.5 M KCl, pH= 7.5, saturated with O_2.

3.4.3. Standard operating procedure of the MHQ device

With isopentane as a liquid cryomedium, the standard operating procedure of the MHQ device is as follows (see Fig. 2). Between the sample preparation events, the mixer is continuously purged at a low flow rate (0.2–0.4 ml min^{-1}) with a sample-free anaerobic carrier solvent, 10 mM NaCl, which is delivered by two HPLC pumps, installed in parallel (Fig. 2-4, 13-1, 13-2). The solvent is kept anoxic by continuous bubbling of Ar gas (Fig. 2-16) through the solvent container (Fig. 2-14). Addition of salt prevents accumulation of static electricity on the jet (Fig. 2-5), and jet break-up due to electrostatic repulsion. Anaerobic conditions minimize orifice clogging, perhaps due to minimal oxidation of the hastalloy mixer surfaces. In the mixer purging mode, the carrier solvent is collected in a container (Fig. 2-6), which is placed inside the ~ 50-l chamber admitted to atmospheric pressure (Fig. 2-1). Just before evacuation (< 0.5 min), 75 ml of a cold cryomedium quencher (isopentane or ethane at 125 K) is poured into a pre-cooled (77 K) vial (Fig. 2-7), which is placed inside the chamber next to the solvent collection container. Immediately after that, the chamber is evacuated using a RV5 oil vacuum pump (Fig. 2-15). During evacuation (2–3 min), the solvent flow rate is increased to the desired value. The AGC controller is programmed to maintain the pressure in the chamber between 100 and 120 mbar. After the pressure in the system reaches this value, the samples are injected in 1:1 ratio into the mixer via the two Rheodyne-type injection valves (Fig. 2-12). To increase the quality of the sample plug-flow, the injection valves are connected to the mixer with a small-inner-diameter PEEK HPLC tubing. Before entering the mixer, both "enzyme" and "substrate" solutions pass through 5- and 0.2-μm in-line solvent filters (Fig. 2-11) installed between the valves and the mixer. The volume of one of the reaction components (substrate) is taken roughly fivefold larger than the volume of the other component (enzyme) (1.5 vs. 0.3 ml), and the substrate is injected first with a short advance (~ 0.5 ml). In this way the mixing chamber is purged with the substrate before the enzyme arrival, so that the substrate concentration in the mixing chamber is constant during the enzyme injection, providing, at excess of the substrate, pseudo-first order reaction conditions, and mixing of the reaction components at 1:1 ratio.

To collect the sample, the mixer, attached to a swinging arm (Fig. 2-3), is rotated inside the low-pressure chamber from spraying into the solvent container to spraying into the vial containing vigorously mixed cryomedium (Fig. 2-8). After collection, the mixer is returned back to spray in the solvent container, and the air is admitted. The whole procedure takes 3–5 min, depending on the sample flow rate. During the sample preparation, the cryomedium warms up by ~ 25–30 degrees to 150–155 K. After air admission, the cryomedium slurry containing MHQ sample is rapidly transferred to a pre-cooled Beckman ultracentrifuge tube (77 K) and immersed in the cold isopentane bath equilibrated at 125 K. The next sample is prepared accordingly.

3.4.4. Sample packing and analysis

Optical absorbance spectroscopy. The 77 K optical absorbance spectroscopic analysis was carried out using an SLM-Aminco DW-2000 scanning spectrophotometer in the split-beam mode equipped with a low-temperature spectroscopy set up. The sample suspension in isopentane (~ 600 μl of myoglobin–azide mixture per ~ 75 ml of isopentane) was used for spectral analysis directly without additional treatment (e.g. sample concentration). The appropriate 2 × 1-ml sample/reference cuvette holder was pre-equilibrated to 77 K under LN_2. The sample-isopentane suspension was rapidly (< 1–2 s) pipetted from the storage tube into the cuvette using a pre-cooled Eppendorf pipette tip (1 ml, blue). The reference cuvette was filled with the buffer-isopentane suspension accordingly. Isopentane was allowed to freeze, and the cuvette holder was transferred to the spectrophotometer for recording of the spectrum.

X-band EPR. EPR spectra were recorded on a Varian E9 spectrometer equipped with a home built He-flow system [249]. In our hands it proved impossible to pack the fine suspension of the MHQ sample into the X-band EPR tube (4-mm i.d.) using any conventional means, e.g. steel-rod packing [49,130] or pressure-filtering [250]. To overcome this problem, a cold centrifugation setup, employing 6 L-M Beckman centrifuge equipped with a wind-shielded 6 × 1-l swing-out rotor, has been assembled. A homemade Al holder for the sample and EPR tube was designed and machined (Fig. 20). In addition, EPR tubes were cut to ~ 6-cm length to fit into the holder. To accommodate the holder in the swingout bucket, an additional adapter was machined as well. For sample packing by cold centrifugation, the holder with the mounted EPR tube and the swing-out buckets are pre-equilibrated to 77 K under LN_2. The holder is incompletely immersed in LN_2 to avoid accumulation of liquid nitrogen inside the holder and/or EPR tube. Just before centrifugation, the sample suspension in isopentane (~ 30 ml) is rapidly poured inside the holder. Almost simultaneously, the swing-out buckets are with-

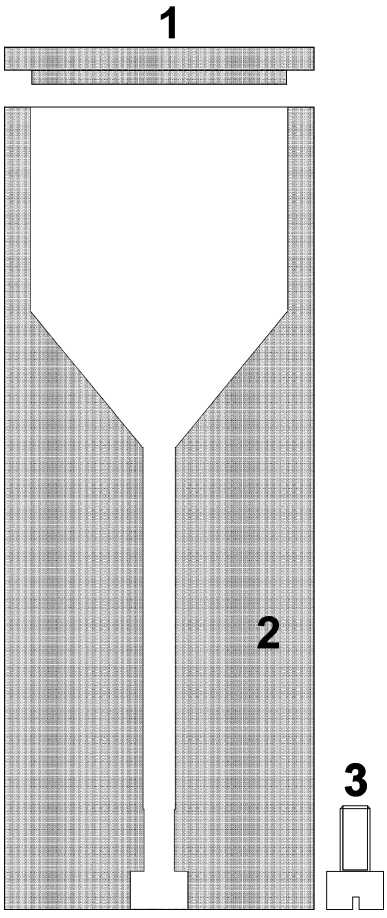

Fig. 20. EPR tube holder for concentration/packing of the sample suspension in the cold centrifugation setup. 1—Polypropylene lid; 2—holder body machined in solid Al; 3—the stopper-screw. A 60 mm-long EPR tube is placed inside the holder with the screw closed, so that the bottom of the tube rests on the screw end. The holder with EPR tube is pre-cooled to 77 K, ~ 30 ml of sample slurry is poured inside the "funnel" top, the lid is closed, and the sample is packed by centrifugation as described in Experimental procedures. For further comments, see text.

drawn from LN_2 and placed in the rotor, ~ 3 l of LN_2 is poured inside the wind shield, the holder(s) with the sample(s) are placed in the rotor, the windshield is closed, and the sample is centrifuged for 5 min at 6000 rpm. Optionally, a stream of cold N_2 gas can be pumped through the centrifugal chamber to prevent warming of the sample. At average, one run takes 6–8 min. Without cold gas flow, the sample warms up during centrifugation to ~ 150–170 K; short time of exposure of the sample to 170 K (1–2 min) does not allow the reaction to proceed further. After centrifugation, the sample holder is placed under LN_2 for 15–20 s. Subsequently, the screw on the bottom of the holder is removed; the EPR tube with the sample is pushed out with the metal rod through the opening in the bottom, and placed in LN_2 for the further storage. Between the sample centrifugation events, the centrifuge is allowed to equilibrate to RT to prevent damage of the motor and electronics.

3.5. Stopped-flow experiments

Transient state kinetic experiments were performed on the Bio Sequential Stopped-Flow Reaction Analyzer SX-18 MV (Applied Photophysics, Leatherhead, UK) using an ozone-free 150-W xenon arc light source. For the kinetic experiments, horse heart metmyoglobin was diluted in the buffer of the appropriate pH to a concentration of 22 μM (11 μM after mixing). All metmyoglobin stocks were stored on ice and used within 1 h after preparation. For the stopped-flow experiments, metmyoglobin and azide stocks were incubated in the syringes for 5 min and mixed at 1:1 ratio. The SX-18 MV software package for the single-wavelength operation mode was used for data acquisition in both absorbance (408 nm), and fluorescence mode. Tryptophan emission was excited at 280 nm and measured as the light passed through a 320-nm cut-off filter. Kinetic traces were obtained by averaging 3–10 shots (optical absorbance at 406 nm) or 10–15 shots in case of protein fluorescence emission under conditions when the observed rate constant did not exceed 800 s^{-1}. The number of shots was increased to measure faster binding, and in some cases up to 150–200 traces were used for averaging.

3.6. Mixing efficiency assay

The mixing efficiency was assayed by following the quenching of the fluorescence emission in the course of protonation of 2-hydroxycinnamic acid (2-HCA). For the assay, the 0.5 μM 2-HCA solution in H_2O, or in the water–glycerol solution at concentrations indicated in the text, was used at pH = 9.5. Fluorescence was quenched by mixing the 2-HCA solution with 20 mM HCl. Fluorescence emission was monitored using a Zeiss Axioplan 2 Trinocular Epi-Fluorescence Research Microscope with Transmitted Light Brightfield and Phase Contrast, equipped with the Epiplan LD objective, $50\times/0.50$ $d = 0$, $a = 6.9$ mm, and 450–600-nm filter. To digitize the image, a Hitachi CCD camera and the Leica Qfluoro v. 1.1 software package were used. The mixer was positioned under the microscope so that the point of observation was directed at the point of exit of the jet from the mixer, i.e. ~ 0.8–1 mm away from the orifice in the platinum inlay. The focal depth of the objective is ± 2 μm; the objective was focused on the center of the jet in the direction perpendicular to the vector of the jet velocity. The resulting image represents a radial slice through the jet with a focal thickness of ~ 4 μm and a length along the propagation direction of ~ 0.1 mm (see also Fig. 5). At 187 m s^{-1} jet speed, the temporal slit width of the observation field is ~ 0.5 μs.

The mixing efficiency was calculated by comparing the values of total light intensity of the acquired images. Total light intensity was calculated by integration of the pixel intensity values from the corresponding image.tif file. Approximately 50–60 images obtained under identical con-

ditions were averaged to obtain the intensity value at a given glycerol concentration. The average intensity of the 2-HCA solution mixed with water was taken as 100% intensity (I_{max}). The average intensity of water (or water/glycerol mixture) mixed with 20 mM HCl (I_{min}) was taken as 0% intensity. The mixing efficiency ($\eta_{\%}$) has been calculated at each glycerol concentration from the average intensity of 2-HCA solution mixed with 20 mM HCl (I_{mix}) using the following correlation.

$$\eta_{\%} = \frac{I_{mix} - I_{min}}{I_{max} - I_{min}} \times 100$$

3.7. Data analysis

Processing of the spectral and/or stopped-flow data, analysis, fitting, and minimization was performed in the Igor Pro v. 4.16 software package (Wavemetrics). Error estimates for the data in graphs and tables represent the standard deviation values.

3.7.1. Weighted fitting of the EPR spectra with a high-term polynomial function

To subtract a baseline in the EPR spectra the following procedure was followed. A spectrum was created of the same field range as the EPR spectra of interest, and filled with artificial ''standard deviation'' values. A low standard deviation value was assigned to the field regions of the spectrum of interest that contain no informative signals, while a 30-fold higher deviation was set for all regions where the resonances are located. For metmyoglobin, the areas of HS and LS resonances were chosen by eye from two high signal-to-noise spectra (at ~ 2 mM metmyoglobin species); for each signal ~ 1.5 times the peak width around the peak maximum was taken. The thus obtained artificial ''standard deviation'' spectrum, which contains low deviation values in the baseline regions and high deviation values in the resonance regions, was used for the weighted polynomial fitting. In the weighted fitting procedure with a high-term polynomial function $k_0 + k_1x + k_2x^2 + \ldots + k_nx^n$, every data point of the spectrum of interest was analyzed by a singular value decomposition fitting algorithm according to its ''weight''—a standard deviation value that was stored in the artificial ''standard deviation'' spectrum. As a result, the high-term polynomials were fitted to the regions of the spectrum with low standard deviation values that contain broad baseline curvatures (Fig. 9A, dotted traces). On the other hand, the informative regions of the spectrum containing sharp HS and LS signals were ''excluded'' from the fitting procedure because of their high standard deviation values, and, basically, a linear regression was fitted to these regions. Thus, the output fitting residuals (Fig. 9B and C) preserve maximum information from the ''signal'' regions, while the off-peak areas essentially converge to the instrument noise around zero.

Acknowledgements

SdV acknowledges the support from The Netherlands Research Organization (NWO grants 98014 and 700-50-025). The authors are grateful to Messrs. A. van de Berg, R. Suijkerbuijk, J.J. Jansen, J. Langeveld, P.J. Vetter, and especially to A. van Adrichem for their advices in designing and machining the micro-mixer. We also greatly acknowledge the gift by Dr. R.B. Gennis of *E. coli* strain GO105, which overproduces the recombinant cytochrome bo_3. We further thank Dr. P. Moënne-Loccoz for performing resonance Raman spectroscopy, Dr. Ir. R.F. Mudde and Dr. Ir. J. Derksen for the LDA experiments, and M.J.F. Strampraad, A.J. Mulder, Msc A.S. Gandhum and Ir. F.G.M. Wiertz for their help in cultivation of microorganisms, enzyme purification and assistance in some MHQ experiments.

This work was supported by NWO (grants 98014 and 700-50-025).

References

[1] E. Fischer, Ber. Dtsch. Chem. Ges. (Berichte der Deutschen Chemischen Gesellschaft) 27 (1894) 2985–2993.
[2] L. Michaelis, M.L. Menten, Biochem. Z. (Biochemische Zeitschrift) 49 (1913) 333–369.
[3] A. Fersht, Structure and Mechanism in Protein Science. A Guide to Enzyme Catalysis and Protein Folding, Freeman, NY, 1999.
[4] I.H. Segel, Enzyme Kinetics : Behavior and Analysis of Rapid Equilibrium and Steady-State Enzyme Systems, Wiley-Interscience Publication, John Wiley & Sons, Inc., New York, Chichester, Brisbane, 1993.
[5] R.M. Daniel, R.V. Dunn, J.L. Finney, J.C. Smith, Annu. Rev. Biophys. Biomol. Struct. 32 (2003) 69–92.
[6] P.K. Agarwal, S.R. Billeter, P.T. Rajagopalan, S.J. Benkovic, S. Hammes-Schiffer, Proc. Natl. Acad. Sci. U. S. A. 99 (2002) 2794–2799.
[7] A.J. Wand, Nat. Struct. Biol. 8 (2001) 926–931.
[8] A.G. Krushelnitsky, V.D. Fedotov, J. Biomol. Struct. Dyn. 11 (1993) 121–141.
[9] N.H. Pawley, J.D. Gans, L.K. Nicholson, J. Biomol. NMR 24 (2002) 215–229.
[10] A.A. Kossiakoff, Methods Enzymol. 131 (1986) 433–447.
[11] F.A. Mulder, N.R. Skrynnikov, B. Hon, F.W. Dahlquist, L.E. Kay, J. Am. Chem. Soc. 123 (2001) 967–975.
[12] W.L. Hubbell, D.S. Cafiso, C. Altenbach, Nat. Struct. Biol. 7 (2000) 735–739.
[13] M. Gerstein, A.M. Lesk, C. Chothia, Biochemistry 33 (1994) 6739–6749.
[14] L.E. Kay, Nat. Struct. Biol., (Suppl. 5) (1998) 513–517.
[15] L.E. Kay, Biochem. Cell. Biol. 76 (1998) 145–152.
[16] R. Ishima, D.A. Torchia, Nat. Struct. Biol. 7 (2000) 740–743.
[17] A.K. Dunker, J.D. Lawson, C.J. Brown, R.M. Williams, P. Romero, J.S. Oh, C.J. Oldfield, A.M. Campen, C.M. Ratliff, K.W. Hipps, J. Ausio, M.S. Nissen, R. Reeves, C. Kang, C.R. Kissinger, R.W. Bailey, M.D. Griswold, W. Chiu, E.C. Garner, Z. Obradovic, J. Mol. Graph. Model. 19 (2001) 26–59.
[18] G.G. Hammes, Biochemistry 41 (2002) 8221–8228.
[19] G. Pettersson, Eur. J. Biochem. 184 (1989) 561–566.
[20] T.C. Bruice, S.J. Benkovic, Biochemistry 39 (2000) 6267–6274.
[21] B. Perman, V. Srajer, Z. Ren, T. Teng, C. Pradervand, T. Ursby, D.

Bourgeois, F. Schotte, M. Wulff, R. Kort, K. Hellingwerf, K. Moffat, Science 279 (1998) 1946–1950.
[22] V. Srajer, Z. Ren, T.Y. Teng, M. Schmidt, T. Ursby, D. Bourgeois, C. Pradervand, W. Schildkamp, M. Wulff, K. Moffat, Biochemistry 40 (2001) 13802–13815.
[23] Z. Ren, B. Perman, V. Srajer, T.Y. Teng, C. Pradervand, D. Schotte, F. Schotte, T. Ursby, R. Kort, M. Wulff, K. Moffat, Biochemistry 40 (2001) 13788–13801.
[24] J.T. Kennis, S. Crosson, M. Gauden, I.H. van Stokkum, K. Moffat, R. van Grondelle, Biochemistry 42 (2003) 3385–3392.
[25] S. Crosson, K. Moffat, Proc. Natl. Acad. Sci. U. S. A. 98 (2001) 2995–3000.
[26] L.M. Barter, J.R. Durrant, D.R. Klug, Proc. Natl. Acad. Sci. U. S. A. 100 (2003) 946–951.
[27] J.A. Leegwater, G.R. Durant, D.R. Klug, J. Phys. Chem., B 101 (1997) 7205–7210.
[28] S.I.E. Vulto, A.M. Streltsov, A.Y. Shkuropatov, V.A. Shuvalov, T.J. Aartsma, J. Phys. Chem., B 101 (1997) 7249–7255.
[29] I. Amitani, T. Sakamoto, T. Ando, Biophys. J. 80 (2001) 379–397.
[30] D. Antoniou, S. Caratzoulas, C. Kalyanaraman, J.S. Mincer, S.D. Schwartz, Eur. J. Biochem. 269 (2002) 3103–3112.
[31] S.G. Codreanu, J.E. Ladner, G. Xiao, N.V. Stourman, D.L. Hachey, G.L. Gillil, R.N. Armstrong, Biochemistry 41 (2002) 15161–15172.
[32] R. Cole, J.P. Loria, Biochemistry 41 (2002) 6072–6081.
[33] H. Deng, N. Zhadin, R. Callender, Biochemistry 40 (2001) 3767–3773.
[34] V.A. Feher, J. Cavanagh, Nature 400 (1999) 289–293.
[35] J.C. Ferreon, V.J. Hilser, Protein Sci. 12 (2003) 982–996.
[36] O. Keskin, X. Ji, J. Blaszcyk, D.G. Covell, Proteins 49 (2002) 191–205.
[37] M. Gulotta, H. Deng, R.B. Dyer, R.H. Callender, Biochemistry 41 (2002) 3353–3363.
[38] J.M. Kriegl, A.J. Bhattacharyya, K. Nienhaus, P. Deng, O. Minkow, G.U. Nienhaus, Proc. Natl. Acad. Sci. U. S. A. 99 (2002) 7992–7997.
[39] N. Munagala, V.J. Basus, C.C. Wang, Biochemistry 40 (2001) 4303–4311.
[40] L. Vitagliano, A. Merlino, A. Zagari, L. Mazzarella, Proteins 46 (2002) 97–104.
[41] R. Desamero, S. Rozovsky, N. Zhadin, A. McDermott, R. Callender, Biochemistry 42 (2003) 2941–2951.
[42] S. Rozovsky, A.E. McDermott, J. Mol. Biol. 310 (2001) 259–270.
[43] S. Rozovsky, G. Jogl, L. Tong, A.E. McDermott, J. Mol. Biol. 310 (2001) 271–280.
[44] J. Fanghanel, Angew Chem., Int. Ed. Engl. 42 (2003) 490–492.
[45] E.Z. Eisenmesser, D.A. Bosco, M. Akke, D. Kern, Science 295 (2002) 1520–1523.
[46] P.T. Rajagopalan, S.J. Benkovic, Chem. Rec. 2 (2002) 24–36.
[47] M.J. Osborne, J. Schnell, S.J. Benkovic, H.J. Dyson, P.E. Wright, Biochemistry 40 (2001) 9846–9859.
[48] M.J. Osborne, P.E. Wright, J. Biomol. NMR 19 (2001) 209–230.
[49] D.P. Ballou, Methods Enzymol. 54 (1978) 85–93.
[50] D.P. Ballou, G.A. Palmer, Anal. Chem. 46 (1974) 1248–1253.
[51] R.J. Appleyard, W.A. Shuttleworth, J.N. Evans, Biochemistry 33 (1994) 6812–6821.
[52] S. Oellerich, E. Bill, P. Hildebrandt, Appl. Spectrosc. 54 (2000) 1480–1484.
[53] M.C. Brenner, C.J. Murray, J.P. Klinman, Biochemistry 28 (1989) 4656–4664.
[54] W.J. Ingledew, Methods Mol. Biol. 131 (1999) 87–95.
[55] A.D. Moodie, R.H. Mitchell, W.J. Ingledew, Anal. Biochem. 189 (1990) 103–106.
[56] S. de Vries, S.P. Albracht, J.A. Berden, E.C. Slater, Biochim. Biophys. Acta 681 (1982) 41–53.
[57] S. de Vries, S.P. Albracht, J.A. Berden, C.A. Marres, E.C. Slater, Biochim. Biophys. Acta 723 (1983) 91–103.
[58] M. Boll, G. Fuchs, D.J. Lowe, Biochemistry 40 (2001) 7612–7620.
[59] V. Schunemann, C. Jung, J. Terner, A.X. Trautwein, R. Weiss, J. Inorg. Biochem. 91 (2002) 586–596.
[60] S. Chouchane, S. Girotto, S. Yu, R.S. Magliozzo, J. Biol. Chem. 277 (2002) 42633–42638.
[61] L. Skipper, W.H. Campbell, J.A. Mertens, D.J. Lowe, J. Biol. Chem. 276 (2001) 26995–27002.
[62] E. Murakami, U. Deppenmeier, S.W. Ragsdale, J. Biol. Chem. 276 (2001) 2432–2439.
[63] M.J. Ryle, H.I. Lee, L.C. Seefeldt, B.M. Hoffman, Biochemistry 39 (2000) 1114–1119.
[64] L. Florens, B. Schmidt, J. McCracken, S. Ferguson-Miller, Biochemistry 40 (2001) 7491–7497.
[65] S. Yu, S. Girotto, X. Zhao, R.S. Magliozzo, J. Biol. Chem. 278 (2003) 44121–44127.
[66] A. Ivancich, H.M. Jouve, B. Sartor, J. Gaillard, Biochemistry 36 (1997) 9356–9364.
[67] T. Brittain, A.R. Baker, C.S. Butler, R.H. Little, D.J. Lowe, C. Greenwood, N.J. Watmough, Biochem. J. 326 (Pt 1) (1997) 109–115.
[68] V. Bandarian, R.R. Poyner, G.H. Reed, Biochemistry 38 (1999) 12403–12407.
[69] A.R. Hurshman, C. Krebs, D.E. Edmondson, B.H. Huynh, M.A. Marletta, Biochemistry 38 (1999) 15689–15696.
[70] L. Dubois, R. Caspar, L. Jacquamet, P.E. Petit, M.F. Charlot, C. Baffert, M.N. Collomb, A. Deronzier, J.M. Latour, Inorg. Chem. 42 (2003) 4817–4827.
[71] S.K. Lee, S.D. George, W.E. Antholine, B. Hedman, K.O. Hodgson, E.I. Solomon, J. Am. Chem. Soc. 124 (2002) 6180–6193.
[72] J.P. Evans, K. Ahn, J.P. Klinman, J. Biol. Chem. 278 (2003) 49692–49698.
[73] W. Zhang, K.K. Wong, R.S. Magliozzo, J.W. Kozarich, Biochemistry 40 (2001) 4123–4130.
[74] A. Koppenhofer, R.H. Little, D.J. Lowe, S.J. Ferguson, N.J. Watmough, Biochemistry 39 (2000) 4028–4036.
[75] B.E. Schultz, D.E. Edmondson, S.I. Chan, Biochemistry 37 (1998) 4160–4168.
[76] J.B. Lynch, C. Juarez-Garcia, E. Munck, L. Que Jr., J. Biol. Chem. 264 (1989) 8091–8096.
[77] C.L. Atkin, L. Thelander, P. Reichard, G. Lang, J. Biol. Chem. 248 (1973) 7462–7464.
[78] B.J. Wallar, J.D. Lipscomb, Chem. Rev. 96 (1996) 2625–2657.
[79] K.E. Liu, S.J. Lippard, in: G. Sykes (Ed.), Advances in Inorganic Chemistry, vol. 42, Academic Press, San Diego, CA, 1995, pp. 263–289.
[80] J.D. Lipscomb, Annu. Rev. Microbiol. 48 (1994) 371–399.
[81] G.N. Jameson, W. Jin, C. Krebs, A.S. Perreira, P. Tavares, X. Liu, E.C. Theil, B.H. Huynh, Biochemistry 41 (2002) 13435–13443.
[82] P. Moënne-Loccoz, C. Krebs, K. Herlihy, D.E. Edmondson, E.C. Theil, B.H. Huynh, T.M. Loehr, Biochemistry 38 (1999) 5290–5295.
[83] A.S. Pereira, W. Small, C. Krebs, P. Tavares, D.E. Edmondson, E.C. Theil, B.H. Huynh, Biochemistry 37 (1998) 9871–9876.
[84] B.G. Fox, J. Shanklin, C. Somerville, E. Munck, Proc. Natl. Acad. Sci. U. S. A. 90 (1993) 2486–2490.
[85] B.G. Fox, J. Shanklin, J. Ai, T.M. Loehr, J. Sanders-Loehr, Biochemistry 33 (1994) 12776–12786.
[86] A.L. Feig, S.J. Lippard, Chem. Rev. 94 (1994) 759–805.
[87] J.M. Bollinger Jr., D.E. Edmondson, B.H. Huynh, J. Filley, J.R. Norton, J. Stubbe, Science 253 (1991) 292–298.
[88] J. Baldwin, C. Krebs, B.A. Ley, D.E. Edmondson, B.H. Huynh, J.M. Bollinger Jr., J. Am. Chem. Soc. 122 (2000) 12195–12206.
[89] C. Krebs, B.H. Huynh, in: G.C. Ferreira, J.J.G. Moura, R. Franco (Eds.), Iron Metabolism, Wiley, Weinheim, Germany, 1999, pp. 253–273.
[90] K.E. Liu, A.M. Valentine, D. Wang, B.H. Huynh, D.E. Edmondson, A. Salifoglou, S.J. Lippard, J. Am. Chem. Soc. 117 (1995) 10174–10185.

[91] J.E. Morgan, M.I. Verkhovsky, G. Palmer, M. Wikstrom, Biochemistry 40 (2001) 6882–6892.
[92] B.C. Hill, C. Greenwood, P. Nicholls, Biochim. Biophys. Acta 853 (1986) 91–113.
[93] B.C. Hill, J. Biol. Chem. 269 (1994) 2419–2425.
[94] B.C. Hill, J. Bioenerg. Biomembranes 25 (1993) 115–120.
[95] B.C. Hill, J. Biol. Chem. 266 (1991) 2219–2226.
[96] B.M. Sjoberg, P. Reichard, A. Graslund, A. Ehrenberg, J. Biol. Chem. 252 (1977) 536–541.
[97] B.M. Sjoberg, Struct. Bond. 88 (1997) 139–173.
[98] M. Hogbom, M. Galander, M. Andersson, M. Kolberg, W. Hofbauer, G. Lassmann, P. Nordlund, F. Lendzian, Proc. Natl. Acad. Sci. U. S. A. 100 (2003) 3209–3214.
[99] P. Nordlund, H. Eklund, J. Mol. Biol. 232 (1993) 123–164.
[100] J. Stubbe, Nature 370 (1990) 502.
[101] M. Ekberg, M. Sahlin, M. Eriksson, B.M. Sjoberg, J. Biol. Chem. 271 (1996) 20655–20659.
[102] J. Stubbe, J. Biol. Chem. 265 (1990) 5329–5332.
[103] J. Stubbe, W.A. van der Donk, Chem. Biol. 2 (1995) 793–801.
[104] S. Licht, G.J. Gerfen, J. Stubbe, Science 271 (1996) 477–481.
[105] J.M. Bollinger Jr., W.H. Tong, N. Ravi, B.H. Huynh, D.E. Edmondson, J. Stubbe, J. Am. Chem. Soc. 116 (1994) 8024–8032.
[106] D. Yun, C. Krebs, G.P. Gupta, D.F. Iwig, B.H. Huynh, J.M. Bollinger Jr., Biochemistry 41 (2002) 981–990.
[107] C. Krebs, S. Chen, J. Baldwin, B.A. Ley, U. Patel, D.E. Edmondson, B.H. Huynh, J.M. Bollinger Jr., J. Am. Chem. Soc. 122 (2000) 12207–12219.
[108] A.M. Valentine, S.S. Stahl, S.J. Lippard, J. Am. Chem. Soc. 121 (1999) 3876–3887.
[109] K.E. Liu, D. Wang, B.H. Huynh, D.E. Edmondson, A. Salifoglou, S.J. Lippard, J. Am. Chem. Soc. 116 (1994) 7465–7466.
[110] W.H. Tong, S. Chen, S.G. Lloyd, D.E. Edmondson, B.H. Huynh, J. Stubbe, J. Am. Chem. Soc. 118 (1996) 2107–2108.
[111] J.M. Bollinger Jr., C. Krebs, A. Vicol, S. Chen, B.A. Ley, B.H. Huynh, J. Am. Chem. Soc. 120 (1998) 1094–1095.
[112] P. Nordlund, H. Eklund, Curr. Opin. Struct. Biol. 5 (1995) 758–766.
[113] L. Que Jr., Y. Dong, Acc. Chem. Res. 29 (1996) 190–196.
[114] B.C. Hill, C. Greenwood, Biochem. J. 215 (1983) 659–667.
[115] N. Ravi, J.M. Bollinger Jr., B.H. Huynh, J. Stubbe, D.E. Edmondson, J. Am. Chem. Soc. 116 (1994) 8007–8014.
[116] B.E. Sturgeon, D. Burdi, S. Chen, B.H. Huynh, D.E. Edmondson, J. Stubbe, B.M. Hoffman, J. Am. Chem. Soc. 118 (1996) 7551–7557.
[117] J.M. Bollinger Jr., W.H. Tong, N. Ravi, B.H. Huynh, D.E. Edmondson, J. Stubbe, Methods Enzymol. 258 (1995) 278–303.
[118] J.M. Bollinger Jr., W.H. Tong, N. Ravi, B.H. Huynh, D.E. Edmondson, J. Stubbe, J. Am. Chem. Soc. 116 (1994) 8015–8023.
[119] M. Kolberg, G. Bleifuss, B.M. Sjoberg, A. Graslund, W. Lubitz, F. Lendzian, G. Lassmann, Arch. Biochem. Biophys. 397 (2002) 57–68.
[120] M. Kolberg, G. Bleifuss, A. Graslund, B.M. Sjoberg, W. Lubitz, F. Lendzian, G. Lassmann, Arch. Biochem. Biophys. 403 (2002) 141–144.
[121] J.M. Bollinger Jr., J. Stubbe, B.H. Huynh, D.E. Edmondson, J. Am. Chem. Soc. 113 (1991) 6289–6291.
[122] J. Ling, M. Sahlin, B.M. Sjoberg, T.M. Loehr, J. Sanders-Loehr, J. Biol. Chem. 269 (1994) 5595–5601.
[123] P.J. Riggs-Gelasco, L. Shu, S. Chen, D. Burdi, B.H. Huynh, L. Que Jr., J. Stubbe, J. Am. Chem. Soc. 120 (1998) 849–860.
[124] J.-P. Willems, H.I. Lee, D. Burdi, P.E. Doan, J. Stubbe, B.M. Hoffman, J. Am. Chem. Soc. 119 (1997) 9816–9824.
[125] D. Burdi, B.E. Sturgeon, W.H. Tong, J. Stubbe, B.M. Hoffman, J. Am. Chem. Soc. 118 (1996) 281–282.
[126] D. Burdi, J.-P. Willems, P.J. Riggs-Gelasco, W.E. Antholine, J. Stubbe, B.M. Hoffman, J. Am. Chem. Soc. 120 (1998) 12910–12919.
[127] J. Baldwin, C. Krebs, L. Saleh, M. Stelling, B.H. Huynh, J.M. Bollinger Jr., P.J. Riggs-Gelasco, Biochemistry 42 (2003) 13269–13279.
[128] A. Cherepanov, S. de Vries, 6th European Conference on Biological Inorganic Chemistry (EuroBIC), Book of Abstracts, July 29–August 3, Lund, Sweden, 2002, pp. 35.
[129] R.C. Bray, Biochem. J. 81 (1961) 189–193.
[130] R.C. Bray, R. Pettersson, Biochem. J. 81 (1961) 194–195.
[131] R.C. Bray, in: B. Chance, R.H. Eisenhardt, Q.H. Gibson, K.K. Longberg-Holm (Eds.), Rapid Mixing and Sampling Techniques in Biochemistry, Academic Press, New York, 1964, pp. 195–203.
[132] G. Palmer, H. Beinert, in: B. Chance, R.H. Eisenhardt, Q.H. Gibson, K.K. Longberg-Holm (Eds.), Rapid Mixing and Sampling Techniques in Biochemistry, Academic Press, New York, 1964, pp. 205–217.
[133] H. Hartridge, F.J.W. Roughton, Proc. Camb. Philos. Soc. XXIII (1927) 450–460.
[134] M.C. Shastry, S.D. Luck, H. Roder, Biophys. J. 74 (1998) 2714–2721.
[135] P. Regenfuss, R.M. Clegg, Biophys. Chem. 26 (1987) 83–89.
[136] P. Regenfuss, R.M. Clegg, M.J. Fulwyler, F.J. Barrantes, T.M. Jovin, Rev. Sci. Instrum. 56 (1985) 283–290.
[137] G.W. Moskowitz, R.L. Bowman, Science 153 (1966) 428–429.
[138] R.L. Berger, B. Balko, H.F. Chapman, Rev. Sci. Instrum. 39 (1968) 493–498.
[139] R.L. Berger, Biophys. J. 24 (1978) 2–20.
[140] H. Hartridge, F.J.W. Roughton, Proc. R. Soc. Lond., A Math. Phys. Sci. 104 (1923) 376–394.
[141] H. Hartridge, F.J.W. Roughton, Proc. R. Soc. Lond., B. Biol. Sci. 94 (1923) 336–367.
[142] H. Hartridge, F.J.W. Roughton, Proc. Camb. Philos. Soc. XXII (1925) 426–431.
[143] Q.H. Gibson, L. Milnes, Biochem. J. 91 (1964) 161–171.
[144] M. Tanaka, K. Matsuura, S. Yoshioka, S. Takahashi, K. Ishimori, H. Hori, I. Morishima, Biophys. J. 84 (2003) 1998–2004.
[145] K. Matsuura, S. Yoshioka, S. Takahashi, K. Ishimori, T. Mogi, H. Hori, I. Morishima, Biochem. ASAP Articles, (2004) 1–9.
[146] Y. Lin, G.J. Gerfen, D.L. Rousseau, S.R. Yeh, Anal. Chem. 75 (2003) 5381–5386.
[147] E. Mayer, P. Bruggeller, Nature 298 (1982) 715–718.
[148] E. Mayer, J. Microsc. 140 (1985) 3–15.
[149] W.B. Bald, J. Microsc. 143 (1986) 89–102.
[150] W.B. Bald, Inst. Phys. Conf. Ser. No. 93, EUREM 88, vol. 3, Institute of Physics Publications, Bristol and Philadelphia, York, England, 1988, pp. 9–14.
[151] C.A. Tulk, D.D. Klug, R. Branderhorst, P. Sharpe, J.A. Ripmeester, J. Chem. Phys. 109 (1998) 8478–8484.
[152] O. Mishima, H.E. Stanley, Nature 396 (1998) 329–335.
[153] H.E. Stanley, S.V. Buldyrev, O. Mishima, M.R. Sadr-Lahijany, A. Scala, F.W. Starr, J. Phys., Condens. Matter 12 (2000) A403–A412.
[154] P. Boutron, R. Alben, J. Chem. Phys. 62 (1975) 4848–4853.
[155] S.R. Elliott, J. Chem. Phys. 103 (1995) 2758–2761.
[156] J.C. Dore, J. Mol. Struct. 237 (1990) 221–232.
[157] F.W. Starr, M.-C. Bellissent-Funel, H.E. Stanley, arXiv: condensed matter 9811118 (1998) 1–15.
[158] G.P. Johari, A. Hallbrucker, E. Mayer, Nature 330 (1987) 552–553.
[159] R.S. Smith, C. Huang, B.D. Kay, J. Phys. Chem., B 101 (1997) 6123–6126.
[160] R.S. Smith, B.D. Kay, Nature 398 (1999) 788–791.
[161] P. Jenniskens, D.F. Blake, Astrophys. J. 473 (1996) 1104–1113.
[162] A. Hallbrucker, E. Mayer, J. Phys. Chem. 91 (1987) 503–505.
[163] H.L. Bank, K.G. Brockbank, J. Card. Surg. 2 (1987) 137–143.
[164] P. Mazur, Science 168 (1970) 939–949.
[165] D.E. Pegg, Cryo-Lett. 22 (2001) 105–114.
[166] G.M. Fahy, D.R. MacFarlane, C.A. Angell, H.T. Meryman, Cryobiology 21 (1984) 407–426.

[167] J. Villermaux, in: N.D. Cheremisinhoff (Ed.), Encyclopedia of Fluid Mechanics, vol. 2, Gulf Publishing, Houston, 1986, pp. 707–719, Chap. 27.
[168] G. Peintler, A. Nagy, A.K. Horvath, T. Kortvelyesi, I. Nagypal, Phys. Chem. Chem. Phys. 2 (2000) 2575–2586.
[169] A. Einstein, Ann. Phys. 19 (1906) 289–306.
[170] A. Einstein, Ann. Phys. 34 (1911) 591–592.
[171] M. Mooney, J. Coll. Sci. 6 (1951) 162–170.
[172] K. Monkos, Curr. Top. Biophys. 25 (2001) 75–80.
[173] K. Monkos, Biochim. Biophys. Acta 1339 (1997) 304–310.
[174] E. Antonini, M. Brunori, Hemoglobin and Myoglobin in Their Reactions with Ligands, vol. 21, North-Holland Publishing Company, Amsterdam, 1971.
[175] D. Duffey, B. Chance, G. Czerlinski, Biochem. Biophys. Res. Commun. 19 (1965) 423–426.
[176] D. Duffey, B. Chance, G. Czerlinski, Biochemistry 5 (1966) 3514–3520.
[177] G.H. Czerlinski, in: B. Chance, R.W. Estabrook, T. Yonetani (Eds.), Hemes and Hemoproteins, Academic Press, New York, 1966, pp. 195–204.
[178] J. Lin, J. Merryweather, L.B. Vitello, J.E. Erman, Arch. Biochem. Biophys. 362 (1999) 148–158.
[179] M. Coletta, M. Angeletti, G. de Sanctis, L. Cerroni, B. Giardina, Eur. J. Biochem. 235 (1996) 49–53.
[180] G.M. Giacometti, A. Da Ros, E. Antonini, M. Brunori, Biochemistry 14 (1975) 1584–1588.
[181] G.H. Czerlinski, W.E. Moeckel, Arch. Biochem. Biophys. 142 (1971) 591–597.
[182] D.E. Goldsack, W.S. Eberlein, R.A. Alberty, J. Biol. Chem. 241 (1966) 2653–2660.
[183] D.E. Goldsack, W.S. Eberlein, R.A. Alberty, J. Biol. Chem. 240 (1965) 4312–4315.
[184] J.S. Olson, G.N. Phillips Jr., J. Biol. Chem. 271 (1996) 17593–17596.
[185] M.M. Pereira, M. Santana, M. Teixeira, Biochim. Biophys. Acta 1505 (2001) 185–208.
[186] S. de Vries, I. Schröder, Biochem. Soc. Trans. 30 (2002) 662–667.
[187] J.H.M. Hendriks, U. Gohlke, M. Saraste, J. Bioenerg. Biomembranes 30 (1998) 15–24.
[188] I.M. Wasser, S. de Vries, P. Moënne-Loccoz, I. Schröder, K.D. Karlin, Chem. Rev. 102 (2002) 1201–1234.
[189] G.T. Babcock, M. Wikstrom, Nature 356 (1992) 301–309.
[190] S. Ferguson-Miller, G.T. Babcock, Chem. Rev. 96 (1996) 2889–2907.
[191] H. Michel, Nature 402 (1999) 602–603.
[192] M. Wikstrom, Biochim. Biophys. Acta 1458 (2000) 188–198.
[193] D. Zaslavsky, R.B. Gennis, Biochim. Biophys. Acta 1458 (2000) 164–179.
[194] M. Ruitenberg, A. Kannt, E. Bamberg, K. Fendler, H. Michel, Nature 417 (2002) 99–102.
[195] P. Rich, Nature 421 (2003) 583.
[196] J. Abramson, S. Riistama, G. Larsson, A. Jasaitis, M. Svensson-Ek, L. Laakkonen, A. Puustinen, S. Iwata, M. Wikstrom, Nat. Struct. Biol. 7 (2000) 910–917.
[197] S. Iwata, C. Ostermeier, B. Ludwig, H. Michel, Nature 376 (1995) 660–669.
[198] C. Ostermeier, A. Harrenga, U. Ermler, H. Michel, Proc. Natl. Acad. Sci. U. S. A. 94 (1997) 10547–10553.
[199] T. Soulimane, G. Buse, G.P. Bourenkov, H.D. Bartunik, R. Huber, M.E. Than, EMBO J. 19 (2000) 1766–1776.
[200] M. Svensson-Ek, J. Abramson, G. Larsson, S. Tornroth, P. Brzezinski, S. Iwata, J. Mol. Biol. 321 (2002) 329–339.
[201] T. Tsukihara, H. Aoyama, E. Yamashita, T. Tomizaki, H. Yamaguchi, K. Shinzawa-Itoh, R. Nakashima, R. Yaono, S. Yoshikawa, Science 272 (1996) 1136–1144.
[202] S. Yoshikawa, K. Shinzawa-Itoh, R. Nakashima, R. Yaono, E. Yamashita, N. Inoue, M. Yao, M.J. Fei, C.P. Libeu, T. Mizushima, H. Yamaguchi, T. Tomizaki, T. Tsukihara, Science 280 (1998) 1723–1729.
[203] M. Wikstrom, A. Jasaitis, C. Backgren, A. Puustinen, M.I. Verkhovsky, Biochim. Biophys. Acta 1459 (2000) 514–520.
[204] J.W. de Gier, M. Schepper, W.N. Reijnders, S.J. van Dyck, D.J. Slotboom, A. Warne, M. Saraste, K. Krab, M. Finel, A.H. Stouthamer, R.J. van Spanning, J. van der Oost, Mol. Microbiol. 20 (1996) 1247–1260.
[205] A. Kannt, T. Soulimane, G. Buse, A. Becker, E. Bamberg, H. Michel, FEBS Lett. 434 (1998) 17–22.
[206] M. Toledo-Cuevas, B. Barquera, R.B. Gennis, M. Wikstrom, J.A. Garcia-Horsman, Biochim. Biophys. Acta 1365 (1998) 421–434.
[207] G. Schafer, M. Engelhard, V. Muller, Microbiol. Mol. Biol. Rev. 63 (1999) 570–620.
[208] B. Chance, Nature 169 (1952) 215–221.
[209] Q.H. Gibson, C. Greenwood, Biochem. J. 86 (1963) 541–555.
[210] C. Greenwood, Q.H. Gibson, J. Biol. Chem. 242 (1967) 1782–1787.
[211] B. Chance, C. Saronio, J.S. Leigh Jr., J. Biol. Chem. 250 (1975) 9226–9237.
[212] B.C. Hill, Ann. N. Y. Acad. Sci. 550 (1988) 98–104.
[213] B.C. Hill, Biochemistry 35 (1996) 6136–6143.
[214] B.C. Hill, J.J. Hill, R.B. Gennis, Biochemistry 33 (1994) 15110–15115.
[215] D.A. Proshlyakov, M.A. Pressler, G.T. Babcock, Proc. Natl. Acad. Sci. U. S. A. 95 (1998) 8020–8025.
[216] S. Han, Y.C. Ching, D.L. Rousseau, Nature 348 (1990) 89–90.
[217] C. Varotsis, Y. Zhang, E.H. Appelman, G.T. Babcock, Proc. Natl. Acad. Sci. U. S. A. 90 (1993) 237–241.
[218] M. Sassaroli, Y.C. Ching, P.V. Argade, D.L. Rousseau, Biochemistry 27 (1988) 2496–2502.
[219] B. Karlsson, L.E. Andreasson, Biochim. Biophys. Acta 635 (1981) 73–80.
[220] G.M. Clore, L.E. Andreasson, B. Karlsson, R. Aasa, B.G. Malmstrom, Biochem. J. 185 (1980) 155–167.
[221] G.M. Clore, L.E. Andreasson, B. Karlsson, R. Aasa, B.G. Malmstrom, Biochem. J. 185 (1980) 139–154.
[222] J.N. Rumbley, E. Furlong Nickels, R.B. Gennis, Biochim. Biophys. Acta 1340 (1997) 131–142.
[223] A. Puustinen, M.I. Verkhovsky, J.E. Morgan, N.P. Belevich, M. Wikstrom, Proc. Natl. Acad. Sci. U. S. A. 93 (1996) 1545–1548.
[224] M. Wikstrom, Biochemistry 39 (2000) 3515–3519.
[225] M. Wikstrom, J.E. Morgan, J. Biol. Chem. 267 (1992) 10266–10273.
[226] D.A. Proshlyakov, T. Ogura, K. Shinzawa-Itoh, S. Yoshikawa, E.H. Appelman, T. Kitagawa, J. Biol. Chem. 269 (1994) 29385–29388.
[227] C. Varotsis, G.T. Babcock, M. Lauraeus, M. Wikstrom, Biochim. Biophys. Acta 1231 (1995) 111–116.
[228] D.A. Proshlyakov, M.A. Pressler, C. DeMaso, J.F. Leykam, D.L. DeWitt, G.T. Babcock, Science 290 (2000) 1588–1591.
[229] S. Junemann, P. Heathcote, P.R. Rich, Biochim. Biophys. Acta 1456 (2000) 56–66.
[230] S.E. Rigby, S. Junemann, P.R. Rich, P. Heathcote, Biochemistry 39 (2000) 5921–5928.
[231] Y.R. Chen, M.R. Gunther, R.P. Mason, J. Biol. Chem. 274 (1999) 3308–3314.
[232] F. MacMillan, A. Kannt, J. Behr, T. Prisner, H. Michel, Biochemistry 38 (1999) 9179–9184.
[233] Y. Orii, T. Mogi, M. Kawasaki, Y. Anraku, FEBS Lett. 352 (1994) 151–154.
[234] Y. Orii, T. Mogi, M. Sato-Watanabe, T. Hirano, Y. Anraku, Biochemistry 34 (1995) 1127–1132.
[235] A.J. Moody, J.N. Rumbley, W.J. Ingledew, R.B. Gennis, P.R. Rich, Biochem. Soc. Trans. 21 (Pt 3) (1993) 255S.
[236] A.J. Moody, P.R. Rich, Eur. J. Biochem. 226 (1994) 731–737.
[237] T. Brittain, R.H. Little, C. Greenwood, N.J. Watmough, FEBS Lett. 399 (1996) 21–25.

[238] K.M. McCauley, J.M. Vrtis, J. Dupont, W.A. Van der Donk, J. Am. Chem. Soc. 122 (2000) 2403–2404.
[239] M. Fabian, G. Palmer, Biochemistry 34 (1995) 13802–13810.
[240] M. Karpefors, P. Adelroth, A. Namslauer, Y. Zhen, P. Brzezinski, Biochemistry 39 (2000) 14664–14669.
[241] M.R. Blomberg, P.E. Siegbahn, G.T. Babcock, M. Wikstrom, J. Inorg. Biochem. 80 (2000) 261–269.
[242] J.E. Morgan, M.I. Verkhovsky, M. Wikstrom, Biochemistry 35 (1996) 12235–12240.
[243] E. Morild, Adv. Protein Chem. 34 (1981) 93–166.
[244] L. Smeller, Biochim. Biophys. Acta 1595 (2002) 11–29.
[245] E. Paci, Biochim. Biophys. Acta 1595 (2002) 185–200.
[246] J.L. Silva, D. Foguel, C.A. Royer, Trends Biochem. Sci. 26 (2001) 612–618.
[247] K. Heremans, L. Smeller, Biochim. Biophys. Acta 1386 (1998) 353–370.
[248] S. de Vries, M.J. Strampraad, S. Lu, P. Moënne-Loccoz, I. Schröder, J. Biol. Chem. 278 (2003) 35861–35868.
[249] C. von Wachenfeldt, S. de Vries, J. van der Oost, FEBS Lett. 340 (1994) 109–113.
[250] A.L. Tsai, V. Berka, R.J. Kulmacz, G. Wu, G. Palmer, Anal. Biochem. 264 (1998) 165–171.